The development of drug resistance in metastatic tumours under chemotherapy: an evolutionary perspective

Federica Padovano, Chiara Villa

The development of drug resistance in metastatic tumours under chemotherapy: an evolutionary perspective

Federica Padovano * Chiara Villa†

Abstract

We present a mathematical model of the evolutionary dynamics of a metastatic tumour under chemotherapy, comprising non-local partial differential equations for the phenotype-structured cell populations in the primary tumour and its metastasis. These equations are coupled with a physiologically-based pharmacokinetic model of drug administration and distribution, implementing a realistic delivery schedule. The model is carefully calibrated from the literature, focusing on BRAF-mutated melanoma treated with Dabrafenib as a case study. By means of long-time asymptotic and global sensitivity analyses, as well as numerical simulations, we explore the impact of cell migration from the primary to the metastatic site, physiological aspects of the tumour tissues and drug dose on the development of chemoresistance and treatment efficacy. Our findings provide a possible explanation for empirical evidence indicating that chemotherapy may foster metastatic spread and that metastases may be less impacted by the chemotherapeutic agent.

1 Introduction

1.1 Biological context and motivation

In 2022 around 9.7 million of people died for cancer worldwide (World Health Organization, 2022), accounting for approximately 15% of total deaths, making it one of the primary health problems globally. In particular, metastases are responsible for approximately 90% of cancer-related mortality (Gupta and Massagué, 2006; Lambert et al., 2017). These form following a multi-step process comprising the migration of cancer cells from the original site to regional or distant organs and lymph nodes, *e.g.* by accessing the lymphatic or blood vessels. In this latter case the metastatic steps include local invasion of regions surrounding the primary tumour, the cancer-induced formation of new blood vessels to access more nutrients and foster cancer growth, process known as *angiogenesis*, intravasation, survival in the circulatory system and extravasation through vascular walls of distant sites (Lambert et al., 2017). The process of primary tumour cells colonization of other tissues is known as *metastatic spread*, or *primary seeding*, meanwhile when cells return to the original site or an existing metastasis they contribute to *self-seeding* (Nguyen and Massagué, 2007; Pantel and Speicher, 2016). Moreover, if the population in the metastatic site grows and acquires itself the ability to metastasise, it can spread to other sites, phenomenon known as *secondary seeding* (Pantel and Speicher, 2016).

Chemotherapy, *i.e.* the use of cytotoxic drugs to kill cancer cells, is to this day considered the most effective, and thus most widely used, modality of cancer treatment. The development of drug resistance confers a selective advantage upon the cancer cell population, as cancer cells exhibit reduced sensitivity to cytotoxic compounds, and represents a significant challenge in cancer therapies as it often contributes to disease relapse (Dagogo-Jack and Shaw, 2018; Gillies et al., 2012; Gottesman, 2002; Turner and Reis-Filho, 2012; Wang et al., 2019). Despite the efforts put into the development of treatment strategies evading or reverting the development of drug resistance (Bukowski et al., 2020), this process becomes significantly more complex in metastatic cancers, given the exposure of tumours in distinct organs to disparate concentrations of therapeutic agents and environmental factors (Wu et al., 2013). In fact, it has been reported that even if standard chemotherapy effectively controls disease progression at the primary tumour site, it often fails to

*Sorbonne Université, CNRS, Université de Paris, Laboratoire Jacques-Louis Lions UMR 7598, 75005 Paris, France. (federica.padovano@sorbonne-universite.fr)

†Sorbonne Université, CNRS, Université de Paris, Inria, Laboratoire Jacques-Louis Lions UMR 7598, 75005 Paris, France. (chiara.villa.1@sorbonne-universite.fr)

influence metastatic populations (D'Alterio et al., 2020; Parker et al., 2022). Moreover, many studies suggest that there is a strong correlation between treatment resistance and metastatic ability, *i.e.* cancer cells with lower sensitivity to cytotoxic agents usually also manifest enhanced disseminating properties (D'Alterio et al., 2020; Karagiannis et al., 2018; Lambert et al., 2017; Luebker and Koepsell, 2019; Shibue and Weinberg, 2017). Therefore the development of drug resistance in the primary tumour during chemotherapy, even in reversible cases, may favour the persistence of its metastases. Nevertheless, it is still unclear whether metastases are intrinsically more resistant than the primary tumour or if their reduced sensitivity arises because they originate from particularly aggressive cell subpopulations or due to subsequent evolution after dissemination (Lambert et al., 2017). It may therefore be beneficial to test existing hypotheses on the development of drug resistance in metastatic tumours under chemotherapy using proof-of-concept theoretical frameworks.

1.2 Mathematical modelling background

Mathematical modelling is a valuable tool for gaining insights into the mechanisms driving cancer evolution and the emergence of intratumour and intertumour heterogeneity, for simulating complex and long-term dynamics that may take years to observe in real-life settings, and for designing optimised therapeutic strategies. All three objectives share a common aim of paving the way towards precision medicine, *i.e.* the innovative idea of targeting therapies on patients in order to increase their efficacy.

Many mathematical models have been previously employed to describe the different steps of the metastatic cascade, see the review article by Scott et al. (2013b) and references therein. These may focus, for instance, on the development of metastatic phenotypes (Michor and Iwasa, 2006; Michor et al., 2006), their intravasation and extravasation (Brodland and Veldhuis, 2012; Franssen et al., 2019; Ramis-Conde et al., 2009), or extensive cell dissemination and potential evolution of cells from the primary to the metastatic site (Bulai et al., 2023; Diego et al., 2013; Hartung et al., 2014; Newton et al., 2013, 2015; Scott et al., 2013a). Moreover, some of them also investigate the effect of therapeutic treatments, such as chemotherapy, radiotherapy and immunotherapy, alone or combined, on metastatic cancers (Ghaffari et al., 2016; Ocaña-Tienda and Pérez-García, 2024; Schlicke et al., 2021; Sun et al., 2016). Among these, Sun et al. (2016) accounted for the existence of a sensitive and a drug-resistant subpopulation in the primary site. Nevertheless, drug-resistance levels may be better captured on a continuum (Lavi et al., 2014), and phenotypic heterogeneity in the metastatic site may also play an important role in the failure of treatment.

Many studies in literature investigate the adaptive processes that underlie the development of intratumour phenotypic heterogeneity and the emergence of resistance to chemotherapeutic agents, see for instance (Clairambault and Pouchol, 2019; Yin et al., 2019) and references therein. Among these, many works consider models comprising non-local partial differential equations (PDEs) modelling the adaptive dynamics of cancer cell populations structured by a continuous phenotypic trait linked with the cell sensitivity to cytotoxic agents (Chisholm et al., 2016a, 2015; Cho and Levy, 2017, 2018a,b, 2020; Clairambault, 2019; Delitala and Lorenzi, 2011; Lavi et al., 2013; Lorenzi et al., 2016; Villa et al., 2021). These models enabled the study of the progressive development of increasing levels of drug resistance during treatment and the role of intratumour heterogeneity in cancer persistence after therapy. This was also possible thanks to their higher amenability to analytical investigations compared to their stochastic counterparts and the mathematical theory supporting such analysis (Barles et al., 1990; Diekmann et al., 2005; Evans, 2022; Fleming and Souganidis, 1986; Perthame, 2006). Some of these studies further applied optimal control methods in order to explore the most effective treatment strategies (Almeida et al., 2019; Olivier and Pouchol, 2019; Pouchol et al., 2018). While this mathematical framework had not been applied to metastatic tumours prior to this manuscript, Mirrahimi (2012) considered the adaptive dynamics of phenotype-structured populations in communicating patches, further developed with applications to speciation in ecology or host-pathogen interactions (Alfaro et al., 2023; Boussange and Pellissier, 2022; Hamel et al., 2021; Lion et al., 2022; Mirrahimi and Gandon, 2020), which is easily comparable with the scenario of connected primary tumour and metastatic sites.

Pharmacokinetic (PK) modelling effectively captures the time course of the drug concentration according to various administration modes and allows to quantify the relationship between the dose and the *in situ* drug concentration (Ahmed, 2015; Jones and Rowland-Yeo, 2013; Zou et al., 2020). In these models, the body is divided into compartments, also referred to as building blocks, each of which is associated to a variable, or quantity, describing the drug concentration in the block. The compartments are then linked to each other through the drug exchange. This kind of models are usually coupled with a pharmacodynamic

(PD) one, which captures the effect of the drug on the considered disease, and employed to find suitable drug dosing schedules to achieve optimal drug concentrations in the target tissues (Gallo et al., 2004; Moss and Siccardi, 2014; Zhou et al., 2007). Moreover, they can also be expanded to include physiological aspects of the considered tissues, such as as organ blood flow and size, in order to explore their influence on the drug exposure (Gallo et al., 2004; Himstedt et al., 2020).

1.3 Synopsis and paper structure

We propose a mathematical model for the evolutionary dynamics of metastatic tumours under chemotherapy, where physiological differences of the tumour sites are integrated within a PK model of drug delivery. In particular, the model comprises a system of coupled non-local PDEs for the phenotypic distribution of the cancer cells in the primary tumour and the metastatic site, structured by their level of resistance to the chemotherapeutic agent, and ordinary differential equations (ODEs) for the pharmacokinetics. We focus on a biological framework including a primary tumour that already faced angiogenesis and a newly-formed yet growing metastasis, where cancer cells characterised by higher levels of drug resistance are assumed to be more aggressive and thus able to migrate to distant sites at higher rates. We restrict our attention to a highly perfused primary tumour and a metastatic site where cells are proliferating but not yet able to disseminate, as chosen by Sun et al. (2016), exploring different levels of tumour vascularisation for the metastasis.

We specifically consider BRAF-mutated melanoma, which is a form of skin cancer that develops in melanocytes, *i.e.* the cells responsible for melanin production, from the uncontrolled proliferation of cells induced by a mutation of the BRAF gene. Despite its lower incidence, BRAF-mutated melanoma is the most aggressive and lethal among the skin cancers (Cabaco et al., 2022; Sundararajan et al., 2022), particularly due to its high metastatic rate (Budczies et al., 2015). These tumours can spread locally, regionally and distantly, with the most common metastatic sites being skin and subcutaneous tissue, followed by lungs, liver, bones, and brain (Sundararajan et al., 2022). Metastatic melanomas are often treated with the chemotherapeutic agent Dabrafenib, a kinase inhibitor of mutated BRAF. Despite the rapid response, with a median time around 6 weeks, and short-term increase in patient survival, resistance to Dabrafenib persists with a median progression-free survival of approximately 6–8 months (Bowyer et al., 2015). For these reasons, a metastatic BRAF-mutated melanoma under Dabrafenib treatment constitutes the ideal case study to adopt for our model, which we carefully calibrate from the literature employing PK parameter values estimated from *in vivo* and *ex vivo* data from patients.

The paper is organised as follows. In Section 2 we introduce the model assumptions and equations. In Section 3 we carry out a formal asymptotic analysis of evolutionary dynamics. In Section 4 we perform global sensitivity analysis and conduct further numerical investigations, to check the analytical results and explore the role of evolutionary and physiological parameters on the outcome of treatment and the timescale of development of drug resistance. Section 5 concludes the paper and provides a brief overview of the model limitations and possible research perspectives.

2 Description of the model

We present a mathematical model of evolutionary dynamics of a metastatic tumour under chemotherapy, comprising non-local phenotype-structured PDEs for the primary tumour and its metastasis. In order to effectively capture the time course of the drug concentration in each tumour site depending on the administration mode and dose, as well as physiological aspects of each tumour site, we complement the evolutionary dynamics model with a physiologically-based PK model for the drug delivery.

2.1 Evolutionary dynamics model of metastatic cancer

We model the evolution of two tumour cell populations, *i.e.* the primary tumour and its metastasis, exposed to a chemotherapeutic agent. In order to consider a metastasised tumour, we assume that the primary tumour is vascularised and the sites are sufficiently well connected so that the cancer cells in the primary tumour can intravasate and, subsequently, extravasate in the secondary site. The opposite process, known as secondary self-seeding (Scott et al., 2013a) is also allowed. In particular, the metastatisation process is modeled by allowing tumour cells to transition from one site to another (Mirrahimi and Perthame, 2015; Scott et al., 2013a). Building upon the ideas presented by Almeida et al. (2019); Mirrahimi (2012); Villa

et al. (2021), we introduce the variable $y \in [0,1]$, which represents the cell phenotypic state linked to its level of chemoresistance. We assume that the phenotypic variant $y = 1$ endows cells with the highest level of cytotoxic-drug resistance and the greatest migratory abilities. This is motivated by evidence suggesting phenotypes with higher drug resistance are more aggressive, and they are often associated with a higher invasive potential (Shibue and Weinberg, 2017). On the contrary, the state $y = 0$ corresponds to cells with the lowest level of cytotoxic-drug resistance and the lowest migratory abilities.
From now on we will make use of the index $i \in \{1,2\}$ to represent each tumour site. In particular, $i = 1$ corresponds to the primary tumour, while $i = 2$ is the metastasis. The phenotypic distribution of tumour cells at time $t \in [0,\infty)$ and site i is described by the function $n_i(t,y)$. Moreover, at each time t, we define the density of tumour cells in site i as

$$I_i(t) := \int_0^1 n_i(t,y)dy\,, \tag{1}$$

with the corresponding local mean phenotypic state and related variance defined, respectively, as

$$\mu_i(t) := \frac{1}{I_i(t)}\int_0^1 y n_i(t,y)dy \quad \text{and} \quad \sigma_i^2(t) := \frac{1}{I_i(t)}\int_0^1 y^2 n_i(t,y)dy - \mu_i^2(t)\,. \tag{2}$$

The phenotypic distribution of tumour cells in each site, $n_i(t,y)$, is governed by the following non-local PDE with given initial and Neumann boundary conditions:

$$\begin{cases} \partial_t n_i - \beta_i \partial_{yy}^2 n_i = R_i(y,I_i,C_i)n_i + \nu_{j,i}(y)n_j - \nu_{i,j}(y)n_i, \quad i \neq j, \quad \text{in} \quad (0,\infty)\times[0,1] \\ I_i(t) := \displaystyle\int_0^1 n_i(t,y)dy, \\ n_i(0,y) = n_{i,0}(y), \\ \partial_y n_i(t,0) = \partial_y n_i(t,1) = 0\,, \end{cases} \qquad i = 1,2\,. \tag{3}$$

The diffusion term in $(3)_1$ models the effects of spontaneous epimutations, which occur at rate $\beta_i \in \mathbb{R}_{>0}$ (Chisholm et al., 2015; Lorenzi et al., 2016). The non-local reaction term takes into account the effects of cell proliferation, natural death, death due to competition for resources, and the cytotoxic action of the drug. The functional $R_i(y,I_i,C_i) \equiv R_i(y,I_i(t),C_i(t))$, models the fitness of tumour cells in site i in the phenotypic state y and under the local environmental conditions at time t, characterised by the cell density $I_i \equiv I_i(t)$, and the chemotherapeutic agent concentration $C_i \equiv C_i(t)$. Building upon the modelling strategies presented by Almeida et al. (2019); Villa et al. (2021), the fitness function R_i is defined as follow

$$R_i(y,I_i,C_i) := p_i(y) - d_i I_i - k_i(y,C_i). \tag{4}$$

In definition (4) the term $d_i I_i$ translates into mathematical terms the idea that a higher total cell number corresponds to less available resources and space in the system, hence a higher rate of death due to intrapopulation competition. The parameter $d_i \in \mathbb{R}_{>0}$ is related to the local carrying capacity of the tumour. The function $p_i(y)$, also referred to as the background fitness in the absence of treatment, stands for the net proliferation rate of cancer cells in the phenotypic state y and site i, and based on the ideas proposed by Villa et al. (2021) we define it as

$$p_i(y) := \delta_i(1-y^2) + \varphi_i(1-(1-y)^2)\,, \tag{5}$$

where $\delta_i \in \mathbb{R}_{>0}$ represents the maximum background fitness for highly proliferating and drug sensitive cells in site i, while $\varphi_i \in \mathbb{R}_{>0}$ represents the maximum background fitness for weakly proliferating and fully chemoresistant cells in tumour i, and we further assume $\delta_i \gg \varphi_i$. Under definition (5), $p_i(y)$ reaches its minimum at $y = 1$, *i.e.* the phenotypic trait characterised by the highest level of cytotoxic-drug resistance and the slowest proliferation in the absence of a drug, since we assume that slowly proliferating cells are less susceptible to chemotherapy and thus more likely to develop resistance (Chu and Sartorelli, 2004; Corrie, 2011). Meanwhile $k_i(y,C_i)$ is the rate of death induced by the cytotoxic drug, and based on the ideas proposed by Villa et al. (2021), we define

$$k_i(y,C_i) := \frac{\eta_i C_i}{\alpha_i + C_i}(1-y)^2\,, \tag{6}$$

where $\eta_i \in \mathbb{R}_{>0}$ is the maximal death rate of highly drug sensitive phenotypic variants due to the cytotoxic action of the chemotherapeutic agent, and $\alpha_i \in \mathbb{R}_{>0}$ is the Michaelis-Menten constant of the chemotherapeutic agent. Under definition (6), $k_i(y, C_i)$ is a decreasing function of y, *i.e.* the rate of drug-induced death decreases as the level of chemoresistance of the cells increases, and it is null for $y = 1$, consistently with the assumption that such a phenotype is completely resistant to the chemotherapeutic agent. With these definitions, after a little algebra, the fitness function in (4) can be rewritten as

$$R_i(y, I_i, C_i) := a_i(C_i) - b_i(C_i)\big(y - h_i(C_i)\big)^2 - d_i I_i \,, \tag{7}$$

where

$$a_i(C_i) = \delta_i - \frac{\eta_i C_i}{\alpha_i + C_i} + \frac{\big(\varphi_i + \frac{\eta_i C_i}{\alpha_i + C_i}\big)^2}{\delta_i + \varphi_i + \frac{\eta_i C_i}{\alpha_i + C_i}} \,, \quad b_i(C_i) = \delta_i + \varphi_i + \frac{\eta_i C_i}{\alpha_i + C_i} \quad \text{and} \quad h_i(C_i) = \frac{\varphi_i + \frac{\eta_i C_i}{\alpha_i + C_i}}{\delta_i + \varphi_i + \frac{\eta_i C_i}{\alpha_i + C_i}} \,. \tag{8}$$

Here $a_i \equiv a_i(C_i)$ is the maximum fitness, $b_i \equiv b_i(C_i)$ is the non-linear selection gradient, and $h_i \equiv h_i(C_i)$ is the phenotypic trait associated to the maximum fitness corresponding to the chemotherapeutic agent concentration $C_i(t)$. We observe that a higher drug concentration C_i results in a lower maximum fitness a_i because of the greater cytotoxic activity due to the compound, a greater fittest phenotypic trait h_i and a stronger selective pressure on tumour cells, *i.e.* a greater b_i.

The terms $\nu_{i,j}(y)$ and $\nu_{j,i}(y)$ in equation (3) are non-negative functions representing the rate of transition of cells in the phenotypic state y from site i to site $j \neq i$, and vice versa, which depend on the ability of the phenotype to intravasate, survive in the circulation and extravasate, given the connectivity of sites i and j. Motivated by Scott et al. (2013a), we assume that all cells with phenotypic state $y > 0$ can access the bloodstream and reach other sites, and we assume that when cancer cells migrate from one site to the other they maintain their original phenotypic trait (Lambert et al., 2017). Specifically, we define the migration rates as

$$\nu_{j,i}(y) = \hat{\nu}_{j,i} y^2, \quad i \neq j, \tag{9}$$

where $\hat{\nu}_{j,i} \in \mathbb{R}_{>0}$ is the maximum transition rate from site j to site i, with $i \neq j$. Under definition (9), migration is almost absent as $y \to 0$, while the migration rate approaches its maximum value $\hat{\nu}_{j,i}$ as $y \to 1$, *i.e.* cells with higher levels of cytotoxic-drug resistance migrate at more significant rates, consistently with our assumptions (Shibue and Weinberg, 2017).

2.2 PK model for anticancer drug

We employ a PK model in order to better predict the drug concentration in two physiologically different tumour sites, given distinct administration methods and doses. To achieve this, we take into account a five-compartments structure, as shown in Figure 1, comprising the administration site, the central and peripheral compartments, and the primary tumour and metastasis blocks. The administration site allows us to take into account the scenarios of extravascular drug injection, *i.e.* when the compound does not enter directly into the circulating system, *e.g. per os*. The central compartment represents plasma and well-perfused tissues, *i.e.* tissues that receive a rich blood supply relative to their organ weight (Cuenod and Balvay, 2013), such as kidneys, liver, heart, and brain. Meanwhile, the peripheral compartment represents poorly-perfused tissues, such as muscle and skin. The primary tumour and metastasis blocks are included in the model structure for two main purposes: to capture the delay between the drug injection and its therapeutic effect, and to introduce in the model some of the physiological differences that can affect the compound distribution in different tumour sites, specifically the tumour size and its vascularization.
We denote by $C_a(t) \geq 0$ the quantity of administered anticancer drug in the administration site, and let $C_c(t), C_p(t), C_1(t), C_2(t) \geq 0$ denote the drug concentration at time t in the central compartment, peripheral block, primary tumour and metastatic site, respectively. Building upon the ideas of Zou et al. (2020) we adopt a first-order kinetics strategy to describe the drug exchange between compartments. Then the mass balance for the first compartment in the model reads as

$$\begin{cases} \frac{dC_a}{dt} = rF - k_a C_a \,, \\ C_a(0) = 0 \,, \end{cases} \tag{10}$$

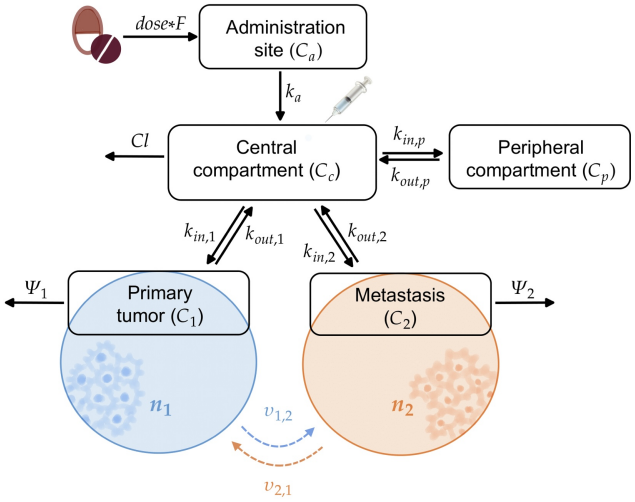

Figure 1: **Schematic of the model.** The five boxes represent the building blocks of the PK model, while the two circles depict the local environment in primary tumour (blue) and metastatic (orange) sites. As illustrated by the overlapping of the boxes and circles, the local environmental conditions in each tumour site will be affected by the drug concentration in the respective PK compartment. The red pills and the grey syringe represent oral administration and intravenous injection, respectively. The straight arrows represent the drug exchange between compartments, while the dashed ones indicate migration of cancer cells. The variables used in the model for the drug concentration in each compartment (C_i) and the phenotypic distribution in each tumour site (n_i) are indicated in the respective box/circle. The parameters and/or functions used in the model to represent the rate of drug or cell flow are indicated next to the respective arrow.

where $F \in (0,1]$ is the bioavailability, *i.e.* the fraction of the administered dose that reaches the systemic circulation, $k_a \in \mathbb{R}_{>0}$ is the absorption rate, and $r \equiv r(t) \geq 0$ is the quantity of administered drug over time. The evolution in time of the drug concentration in the peripheral compartment is given by

$$\begin{cases} \frac{dC_p}{dt} = k_{in,p}C_c - k_{out,p}C_p\,, \\ C_p(0) = 0\,, \end{cases} \tag{11}$$

where $k_{in,p} \in \mathbb{R}_{>0}$ and $k_{out,p} \in \mathbb{R}_{>0}$ are the first-order constant rates of drug concentration respectively entering and exiting the peripheral compartment. The two physiological aspects we want to consider, *i.e.* tumour size and vascularization, are captured by quantities such as tumour volume and *in situ* blood flow. We thus introduce the parameters $V_1, V_2 \in \mathbb{R}_{>0}$ representing the volumes of the primary tumour and the metastasis, respectively, and $Q_1, Q_2 \in \mathbb{R}_{\geq 0}$ representing the blood flows through the primary tumour and metastasis, respectively. We assume the primary tumour site to be more vascularised and thus take $Q_1/V_1 > Q_2/V_2$. In order to set the dependency of the first-order distribution constant rates of the two tumour sites on their physiological features, we take inspiration from the physiologically-based PK models and adopt the *perfusion rate-limited* strategy (Jones and Rowland-Yeo, 2013). This latter assumes that the drug distributes freely and instantly across membranes, hence blood perfusion becomes the only limiting process for the drug distribution in the two tumour sites. Therefore, the ODEs describing the evolution in time of the compound concentration in the primary tumour and its metastasis, are given by

$$\begin{cases} \frac{dC_1}{dt} = \frac{Q_1 R}{V_1}C_c - \frac{Q_1 R}{V_1 K_1}C_1 - \Psi_1\,, \\ C_1(0) = 0\,, \end{cases} \quad \text{and} \quad \begin{cases} \frac{dC_2}{dt} = \frac{Q_2 R}{V_2}C_c - \frac{Q_2 R}{V_2 K_2}C_2 - \Psi_2\,, \\ C_2(0) = 0\,, \end{cases} \tag{12}$$

where the constant $R \in (0,1]$ is the blood-to-plasma drug partition coefficient, and $K_1, K_2 \in (0,1]$ are the tumour-to-plasma partition coefficients for primary tumour and metastasis, respectively. These will affect how the chemical distributes throughout the tissues, w.r.t. the plasma concentration, and are an important part of any pharmacokinetic study. The terms $\Psi_1 \equiv \Psi_1(C_1, n_1)$ and $\Psi_2 \equiv \Psi_2(C_2, n_2)$ model consumption of the the cytotoxic drug by the cancer populations and, following the ideas proposed by Villa et al. (2021),

are defined as

$$\Psi_i(C_i, n_i) := \psi_i \frac{\eta_i C_i(t)}{\alpha_i + C_i(t)} \int_0^1 (1-y)^2 n_i(t,y) dy \quad i = 1, 2\,, \tag{13}$$

where α_i and η_i were introduced in (6), while $\psi_i \in \mathbb{R}_{>0}$ is a conversion factor. Finally, the mass balance equation describing the evolution in time of the drug concentration in the central compartment is given by

$$\begin{cases} \frac{dC_c}{dt} = \frac{k_a}{V_c}\, C_a + \frac{Q_1}{V_b K_1} C_1 + \frac{Q_2}{V_b K_2} C_2 + k_{out,p} C_p - \left(\frac{Cl}{V_c} + \frac{Q_1+Q_2}{V_b} + k_{in,p} \right) C_c\,, \\ C_c(0) = 0\,, \end{cases} \tag{14}$$

where $V_c \in \mathbb{R}_{>0}$ is the volume of the central compartment and $V_b \in \mathbb{R}_{>0}$ is the blood volume. This latter parameter is introduced in the ODE because the tumour sites uptake drug from the circulating system and not from the entire central compartment. Moreover, $Cl \in \mathbb{R}_{>0}$ represents the clearance, *i.e.* the volume of plasma cleared of a drug over a specified time period. Under the scenario of drug infusion, the factor $k_a C_a$ in equation $(14)_1$ will be replaced by the infusion rate.

3 Analysis of evolutionary dynamics

In this section, we study the long-time behaviour of the system (3), *i.e.* its solution for $t \to \infty$, with R_i in the form of (7). To achieve this, we focus on a scenario where the concentration of chemotherapeutic agent is constant in time, *i.e.* the function $C_i(t)$ is given and satisfies the following assumption

$$C_i(t) \equiv c_i \geq 0\,, \quad i \in \{1, 2\}.$$

Consequently, the time dependency of the fitness function is no longer mediated by the drug concentration, and we here make use of the simplified notation $R_i(y, I_i) \equiv R_i(y, I_i, c_i)$, along with $a_i \equiv a_i(c_i)$, $b_i \equiv b_i(c_i)$ and $h_i \equiv h_i(c_i)$ for the factors appearing in (7) and defined in (8).

3.1 Assumptions

Fitness functions R_i We assume there exist positive constants I_m, I_M such that the following hold:

$$\frac{\partial R_i}{\partial I_i}(y, I_i) < 0 \qquad \forall\, y \in [0,1]\,, \quad I_i \in [I_m, I_M]\,, \quad i = 1, 2\,; \tag{15}$$

$$\frac{\partial^2 R_i}{\partial y^2}(y, I_i) < 0 \qquad \forall\, y \in [0,1]\,, \quad I_i \in [I_m, I_M]\,, \quad i = 1, 2\,. \tag{16}$$

We have introduced the natural assumption that growth is saturated by an overall higher population density, due to competition for space and resources, which translates mathematically into (15), *i.e.* each fitness function is a monotonically decreasing function of the local cell density. In addition, we have assumed that in each given local environment there is only one fittest phenotypic trait, which translates mathematically into (16), *i.e.* each fitness function is strictly concave in y and thus presents only one maximum in $[0, 1]$. The fittest function definition we give in (7) satisfies assumptions (15) and (16).

Migration rates $\nu_{i,j}(y)$ We consider generic phenotype-dependent migration rates $\nu_{i,j}(y) \geq 0$, and assume there exist positive constants $\nu_m, \nu_M \in \mathbb{R}_{\geq 0}$ so that $\nu_{i,j}(y)$ satisfy the following properties:

$$0 \leq \nu_m \leq \nu_{i,j}(y) \leq \nu_M < \infty \quad \forall y \in [0,1], \quad i, j = 1, 2\,, \quad i \neq j, \tag{17}$$

$$\nu'_{i,j}(y) \geq 0 \quad \forall y \in [0,1], \quad i, j = 1, 2\,, \quad i \neq j. \tag{18}$$

Property (17) expresses the natural assumption that migration rates from one site to the other are non-negative and bounded for all phenotypic variants. Moreover, we assume that cells with higher levels of cytotoxic-drug resistance migrate to different sites at higher rates (Shibue and Weinberg, 2017), which translates mathematically into (18), *i.e.* the migration rates are increasing functions of the phenotypic state y. Definition (9) for the migration rates satisfies assumptions (17) and (18).

Effective fitness Notice that we may rewrite $(3)_1$ in terms of the effective fitness function $R_i(y, I_i) - \nu_{i,j}(y)$ for $i, j = 1, 2$ $(i \neq j)$. Building on the ideas proposed by Mirrahimi (2012), we assume this is such that

$$\arg\max_{y\in[0,1]} \big[R_i(y, I_i) - \nu_{i,j}(y)\big] \quad \text{is a singleton for} \quad i, j = 1, 2 \quad \text{and} \quad i \neq j\,, \tag{19}$$

$$\arg\max_{y\in[0,1]} \big[R_1(y, I_1) - \nu_{1,2}(y)\big] \cap \arg\max_{y\in[0,1]} \big[R_2(y, I_2) - \nu_{2,1}(y)\big] = \emptyset\,, \tag{20}$$

that is, the effective fitness function of each population allows only one maximum and the traits corresponding to these maxima are distinct.

Additional technical assumptions Following the ideas proposed by Mirrahimi (2012), and given ν_m and ν_M introduced in (17), the analysis will also rely on the additional technical assumption that there exists a constant $\delta > 0$ such that

$$\delta \leq \min\left(R_i\Big(y, \frac{\nu_m}{\nu_M} I_m\Big)\,,\, R_i\Big(y, I_m\Big)\right) \qquad \forall\, y \in [0, 1]\,, \quad i = 1, 2\,, \tag{21}$$

$$\max\left(R_i\Big(y, \frac{\nu_m}{\nu_M} I_M\Big)\,,\, R_i\Big(y, I_M\Big)\right) \leq -\delta \qquad \forall\, y \in [0, 1]\,, \quad i = 1, 2\,. \tag{22}$$

3.2 Hyperbolic time scaling and steady state problem

In accordance with previous studies in literature (Doerfler and Böhm, 2006; Duesberg et al., 2000), we assume the rate of spontaneous phenotypic variations β_i to be small, since these phenomena occur on a slower time scale compared to cell division and death. We therefore introduce a small parameter $\varepsilon > 0$ and assume both $\beta_i := \varepsilon^2$ $(i = 1, 2)$. Following previous studies on the long-time behaviour of non-local PDEs and integro-differential equations modelling the dynamics of continuously structured populations (Barles et al., 2009; Chisholm et al., 2016b; Desvillettes et al., 2008; Diekmann et al., 2005; Jabin and Schram, 2016; Lorz et al., 2011; Mirrahimi and Perthame, 2015; Perthame and Barles, 2008), we use the hyperbolic time scaling $t \mapsto \frac{t}{\varepsilon}$ in the conservation equation (3), and obtain the following system of non-local PDEs for the phenotypic distributions $n_{i\varepsilon}(t, y) = n_i\left(\frac{t}{\varepsilon}, y\right)$ $(i = 1, 2)$:

$$\begin{cases} \varepsilon \partial_t n_{i\varepsilon} - \varepsilon^2\, \partial^2_{yy} n_{i\varepsilon} = R_i\big(y, I_{i\varepsilon}\big)\, n_{i\varepsilon} + \nu_{j,i}(y)\, n_{j\varepsilon} - \nu_{i,j}(y)\, n_{i\varepsilon}\,, \quad i \neq j\,, \\ I_{i\varepsilon}(t) := \displaystyle\int_0^1 n_{i\varepsilon}(t, y)\, \mathrm{d}y \qquad\qquad i = 1, 2\,. \\ \partial_y n_{i\varepsilon}(t, 0) = \partial_y n_{i\varepsilon}(t, 1) = 0 \end{cases} \tag{23}$$

As we are interested in the equilibria of (3) in the case of rare phenotypic variations, we follow the strategy adopted by Mirrahimi (2012) and investigate the equilibria of (23) in the asymptotic regime $\varepsilon \to 0$. Assume that as $t \to \infty$ we have that $n_{i\varepsilon}(t, y) \to n^\infty_{i\varepsilon}(y)$ and $I_{i\varepsilon}(t) \to I^\infty_{i\varepsilon}$ $(i = 1, 2)$. Then, the equilibria of (23) satisfy the following system of non-local ODEs

$$\begin{cases} R_i\big(y, I^\infty_{i\varepsilon}\big)\, n^\infty_{i\varepsilon} + \varepsilon^2\, (n^\infty_{i\varepsilon})'' + \nu_{j,i}(y)\, n^\infty_{j\varepsilon} - \nu_{i,j}(y)\, n^\infty_{i\varepsilon} = 0\,, \quad i \neq j\,, \\ I^\infty_{i\varepsilon} = \displaystyle\int_0^1 n^\infty_{i\varepsilon}(y)\, \mathrm{d}y \qquad\qquad i = 1, 2\,. \\ n^\infty_{i\varepsilon}(0) = n^\infty_{i\varepsilon}(1) = 0 \end{cases} \tag{24}$$

From now on we will make use of the notation $n_{i\varepsilon}(y)$ and $I_{i\varepsilon}$ $(i = 1, 2)$ to refer to $n^\infty_{i\varepsilon}(y)$ and $I^\infty_{i\varepsilon}$, respectively.

3.3 Results of formal analysis

We here summarise the results of the formal analysis, detailed in A, extending the results of Mirrahimi (2012) to the case of phenotype-dependent migration rates between the sites, for our model of evolutionary dynamics of connected metastatic tumours.

Bounds on I It can be shown from (24) that for all $\varepsilon \leq \varepsilon_0$, with ε_0 small enough, under assumptions (15), (17), (21) and (22), we have

$$I_m \leq I_{i\varepsilon} \leq I_M \qquad i = 1, 2\,, \tag{25}$$

for all ε, where we recall $0 < I_m < I_M$. Proof of this follows analogous steps of that in (Mirrahimi, 2012, Lemma 2.1), and can be found in A.1. As a result, in the asymptotic regime $\varepsilon \to 0$ we have $I_{i\varepsilon} \to I_i$ with

$$I_m \leq I_i \leq I_M \qquad i = 1, 2\,. \tag{26}$$

Asymptotic regime $\varepsilon \to 0$ Building on the strategies adopted in (Mirrahimi, 2012), we introduce the Hopf-Cole transformation

$$n_{i\varepsilon}(y) = \exp\left(\frac{u_{i\varepsilon}(y)}{\varepsilon}\right) \qquad i = 1, 2\,, \tag{27}$$

with $u_{i\varepsilon}(y)$ semi-convex (*i.e.* $\partial^2_{yy} u_{i\varepsilon} \geq -E$, for some constant $E > 0$). Then, we expect that $I_{1\varepsilon} \to I_1$, $I_{2\varepsilon} \to I_2$, $u_{1\varepsilon} \to u_1$ and $u_{2\varepsilon} \to u_2$ in the asymptotic regime $\varepsilon \to 0$, where I_1, I_2, u_1 and u_2 are the leading-order terms of the asymptotic expansions for $I_{1\varepsilon}$, $I_{2\varepsilon}$, $u_{1\varepsilon}$ and $u_{2\varepsilon}$, respectively. Assuming that $u_1 = u_2 = u$ and that the semi-convexity of $u_{i\varepsilon}$ $(i = 1, 2)$ is preserved in the limit, so that $u = u(y)$ is also semi-convex, we have that u is a viscosity solution to the following constrained Hamilton-Jacobi equation

$$\begin{cases} -\left(\dfrac{du}{dy}\right)^2 = H(y, I_1, I_2)\,, \\ \max\limits_{y\in[0,1]} u(y) = 0\,, \end{cases} \tag{28}$$

with $H(y, I_1, I_2)$ being the largest eigenvalue of the matrix

$$\mathcal{A} = \begin{pmatrix} R_1\big(y, I_1\big) - \nu_{1,2}(y) & \nu_{2,1}(y) \\ \nu_{1,2}(y) & R_2\big(y, I_2\big) - \nu_{2,1}(y) \end{pmatrix}.$$

Given the assumptions introduced in Section 3.1, from (25) and (26) we deduce that $n_{1\varepsilon}$ and $n_{2\varepsilon}$ converge weakly to measures n_1 and n_2. Moreover, from (28), we have that

$$n_{i\varepsilon}(y) \xrightarrow[\varepsilon\to 0]{*} \sum_{k=1}^{K} \rho_{ik}\, \delta(y - y_k) \qquad i = 1, 2\,, \tag{29}$$

i.e. the measures n_1 and n_2 to which $n_{1\varepsilon}$ and $n_{2\varepsilon}$ converge weakly in the asymptotic regime $\varepsilon \to 0$ concentrate as K Dirac masses centered at y_k $(k = 1, ..., K)$, where the weights $\rho_{ik} \geq 0$ must be such that

$$I_i = \sum_{k=1}^{K} \rho_{ik} \qquad i = 1, 2\,, \tag{30}$$

and where the finite number of points $y_k \in \Omega \cap \Gamma$, with $\Omega := \big\{y \in [0,1] : u(y) = 0\big\}$ and $\Gamma := \big\{y \in [0,1] : H(y, I_1, I_2) = 0\big\}$. Specifically, this yields

$$\begin{cases} \big(R_1(y_k, I_1) - \nu_{1,2}(y_k)\big)\rho_{1k} + \nu_{2,1}(y_k)\rho_{2k} = 0 \\ \big(R_2(y_k, I_2) - \nu_{2,1}(y_k)\big)\rho_{2k} + \nu_{1,2}(y_k)\rho_{1k} = 0 \end{cases} \qquad k = 1, .., K\,. \tag{31}$$

Details of the formal analysis in the asymptotic regime $\varepsilon \to 0$ can be found in A.2.

Analytical results for the metastatic spread case: $\nu_{1,2} \not\equiv 0$ and $\nu_{2,1} \equiv 0$ The long-time solution of our system with the fitness function $R_i(y, I_i)$ defined as in (7) and the migration rate $\nu_{i,j}(y)$ defined as in (9), and obtained by solving (31), is the following:

$$n_1(y) = I_1\, \delta(y - y_1) \qquad \text{and} \qquad n_2(y) = \rho_{21}\, \delta(y - y_1) + \rho_{22}\, \delta(y - y_2)\,, \tag{32}$$

with

$$y_1 = \frac{b_1}{b_1 + \hat{\nu}_{1,2}} h_1\,, \qquad y_2 = h_2\,, \tag{33}$$

and

$$I_1 = \frac{1}{d_1}\left[a_1 - \frac{\hat{\nu}_{1,2} b_1 h_1^2}{b_1 + \hat{\nu}_{1,2}}\right], \quad I_2 = \frac{a_2}{d_2}, \qquad \rho_{21} = \min\left(\frac{\hat{\nu}_{1,2}\, y_1^2}{b_2 (y_1 - h_2)^2} I_1, I_2\right), \quad \rho_{22} = I_2 - \rho_{21}\,. \tag{34}$$

The proof can be found in the A.3, while the results for the localised tumours ($\nu_{1,2} \equiv 0$ and $\nu_{2,1} \equiv 0$) and secondary seeding ($\nu_{1,2} \not\equiv 0$ and $\nu_{2,1} \not\equiv 0$) scenarios can be found in the supplementary sections S.1.1 and S.1.2, respectively.

3.4 Biological insights

The biological interpretation of the results of the formal analysis summarised in Section 3.3 for the metastatic spread case yields interesting biological insights. Figure 2 displays the possible model outcomes, based on the constraints imposed on the migration rates, obtained simulating a non-dimensional version of the model. We particularly focus on the metastatic spread case here, and further illustrate the dependency of the solution on certain parameters in Figure 3, but provide more details on the other biological scenarios in the supplementary material.

Different biological scenarios From the analysis, and as can be seen in Figure 2, we note that:

(i) In the case of a localised tumour, the primary tumour evolves into a monomorphic population, with the selected trait being the fittest locally ($y_1 = h_1$) and the total cell density reaching the carrying capacity of the site ($I_1 = \frac{a_1}{d_1}$), and no metastasis forms (cf. Figure 2A).

(ii) In the case of metastatic spread, from (32) we have that the population in the primary tumour will evolve into a monomorphic population, while the population in the metastatic site will evolve into a dimorphic population (or a monomorphic one under certain conditions, explained later), as also illustrated in Figure 2B.

(iii) In the case of metastatic spread with secondary seeding, dimorphism may be observed in both tumours (cf. Figure 2C) or, in the case of highly connected sites, both tumours may evolve into a monomorphic population adapted to both environments (cf. Figure 2D), although this scenario is unlikely to be observed *in vivo*.

Metastatic spread: the primary site From (32)-(34) we have that the composition and size of the population in the primary tumour not only depend on the local environment but also on the ability of cells to intravasate and eventually metastasise. In particular, we observe the following:

(iv) The selected trait in the primary tumour y_1 is smaller than the locally fittest one h_1, unlike in the localised tumour case. Hence, if cells have different metastatic abilities depending on their phenotypic state, at equilibrium cells less prone to metastasise are found in the primary tumour, probably since the more metastatic phenotypes have left the site.

(v) In particular, y_1 is a decreasing function of $\hat{\nu}_{1,2}$, indicating that the magnitude of this phenotypic shift ($|y_1 - h_1|$) increases with the migration rate.

(vi) The total population at equilibrium in the primary tumour is lower than the carrying capacity of the site, *i.e.* $I_1 < \frac{a_1}{d_1}$, unlike in the case of a localised tumour. Recall however that this comes with the trade off of having established a dimorphic population in the metastatic site, which increases the chances of surviving environmental changes, overall resulting in greater evolutionary advantage.

Metastatic spread: the metastatic site From (32)-(34), we observe that the total cell density of the metastatic tumour reaches carrying capacity, *i.e.* $I_2 = \frac{a_2}{d_2}$, but the contribution of cells coming in from the primary tumour will affect the composition of the local population. In particular, we observe the following:

(vii) We have that ρ_{21} is an increasing function of I_1 and $\hat{\nu}_{1,2}$, suggesting that a larger population in the primary site or a higher migration rate will result in a larger subpopulation in the secondary site presenting traits selected in the primary, as also illustrated in Figure 3 (third column).

(viii) Moreover, if $\hat{\nu}_{1,2}$ is significantly high, this might lead to $\rho_{21} = I_2$ and $\rho_{22} = 0$ (cf. bottom plot in the third column of Figure 3). This means that if the migration rate of cells between sites is particularly high then the subpopulation in the secondary site presenting traits selected in the primary may outnumber the subpopulation with traits adapted to the local environment and drive it to extinction. This scenario can also occur in the case the population density of the primary tumour I_1 is significantly big w.r.t. to the one of the metastasis I_2.

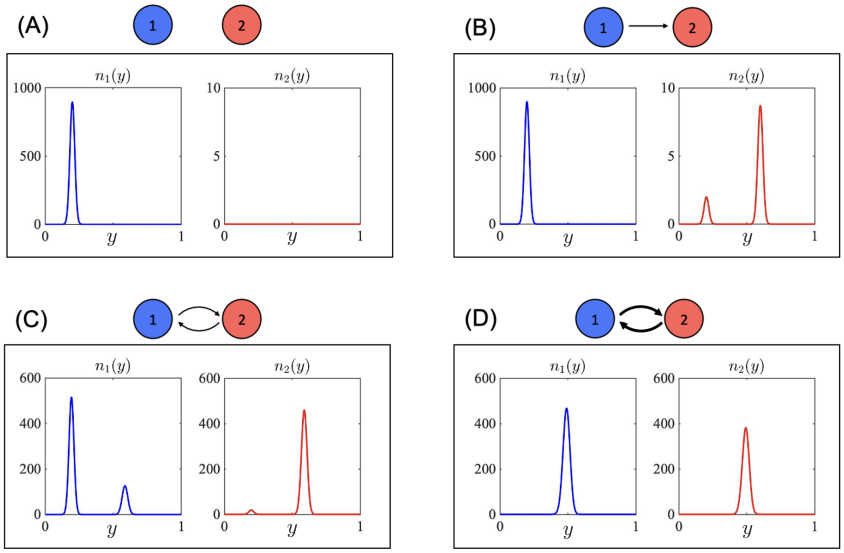

Figure 2: **Model outcome dependency on the migration rates.** Possible model outcomes under different proof-of-concept non-dimensional parameter sets. We simulate system (3), under definition (7) for the fitness functions R_i and definition (9) for the migration rates $\nu_{i,j}(y)$, under the initial conditions $n_{0,1}(y) > 0$ and $n_{0,2}(y) = 0$ $\forall y \in [0,1]$. Each plot displays the equilibrium solution in a different biological scenario: (A) Localised tumour, under the parameter set $\beta_1 = \beta_2 = 10^{-7}$, $a_1 = 8$, $a_2 = 0.1$, $b_1 = 1$, $b_2 = 0.8$, $h_1 = 0.2$, $h_2 = 0.6$, $d_1 = d_2 = 0.2$, and $\hat{\nu}_{1,2} = \hat{\nu}_{2,1} = 0$; (B) Metastatic spread, under the parameter set of A, except $\hat{\nu}_{1,2} = 0.007$; (C) Secondary seeding, under the parameter set $\beta_1 = \beta_2 = 10^{-7}$, $a_1 = 6$, $a_2 = 5$, $b_1 = 1$, $b_2 = 0.6$, $h_1 = 0.2$, $h_2 = 0.6$, $d_1 = d_2 = 0.2$, $\hat{\nu}_{1,2} = 0.1$ and $\hat{\nu}_{2,1} = 0.05$. (D) Secondary seeding in highly connected sites, under the parameter set of C except $\hat{\nu}_{1,2} = 0.6$ and $\hat{\nu}_{2,1} = 0.3$.

(ix) We have that ρ_{21} is a decreasing function of the non-linear selection gradient b_2, suggesting that a stronger selective pressure from the environment in the secondary site will result in a smaller local subpopulation presenting traits selected in the primary, as also shown in Figure 3 (first column).

(x) Moreover, in the limit $b_2 \to \infty$ we have $\rho_{21} \to 0$ (cf. bottom plot in the first column of Figure 3). This means that in the case of extremely strong selective pressure, assuming cells from the primary site already managed to create a local niche in the metastatic site, this will eventually only evolve into a monomorphic population, as the trait selected in the primary site will not be fit enough to survive.

(xi) Finally, ρ_{21} is a decreasing function of the distance between y_1 and h_2, indicating that the closer the selected trait in the primary site is to the fittest trait of the metastatic site, the higher the subpopulation density in the metastatic site of cells presenting the trait selected in the primary site is. This may depend on the shift in the phenotypic trait selected in the primary site compared to the fittest one in the local environment h_1, but also on the similarity of environmental condition in the two sites, *i.e.* the distance $|h_1 - h_2|$, as also illustrated in Figure 3 (second column).

4 Numerical results

We complement the analytical results presented in Section 3 with numerical solutions of the model equations, focusing on the metastatic spread case and under dynamic drug concentrations as predicted by the PK model, *i.e.* we solve system (3), under definitions (4) and (7)-(9), coupled with equations (10)-(14).

In Section 4.1 we present the set-up and parameter values employed for the numerical simulations, along with the numerical method employed to simulate the model. In Section 4.2 we perform global sensitivity analysis of the model equations, while in Section 4.3 we investigate how the parameters impact the model outcome, that is, the equilibrium solution of the system of equations, and the time it takes for the system to reach steadiness, in view of the relative impact this may have during the course of treatment.

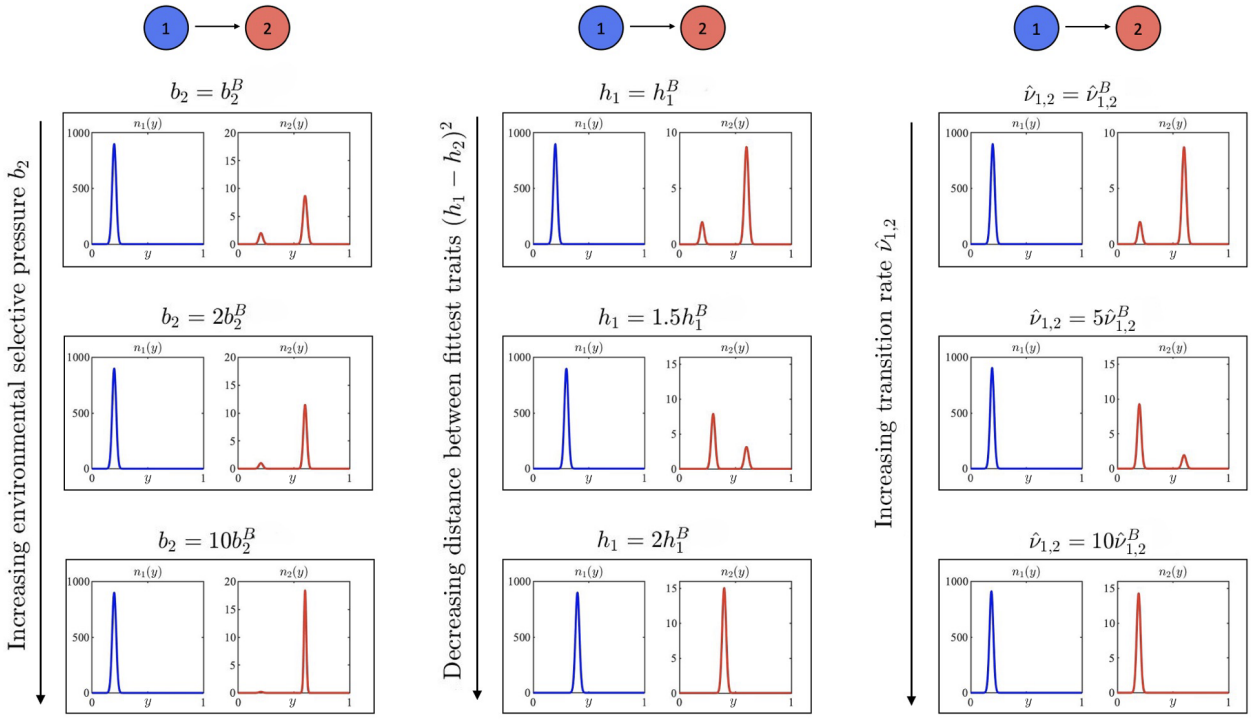

Figure 3: **Model outcome dependency on input factors in the metastatic spread scenario.** Illustrative example showing how the selection gradient b_2, the fittest trait h_1 and the maximum migration rate $\hat{\nu}_{1,2}$ may affect the equilibrium distributions of the cancer cell populations of each site, in the metastatic spread case. We simulate system (3), under definition (7) for the fitness functions R_i and definition (9) for the migration rates $\nu_{i,j}(y)$, under the initial conditions $n_{0,1}(y) > 0$ and $n_{0,2}(y) = 0$, $\forall y \in [0,1]$. Each column displays the equilibrium solutions of three simulations obtained by progressively varying the parameters b_2 (first column), h_1 (second column) and $\hat{\nu}_{1,2}$ (third column) form their baseline values $b_2^B = 0.8$, $h_1^B = 0.2$ and $\hat{\nu}_{1,2}^B = 0.007$. The remaining parameters are set to $\beta_1 = \beta_2 = 10^{-7}$, $a_1 = 8$, $a_2 = 0.1$, $b_1 = 1$, $b_2 = b_2^B$, $h_1 = h_1^B$, $h_2 = 0.6$, $d_1 = d_2 = 0.2$, $\hat{\nu}_{1,2} = \hat{\nu}_{1,2}^B$ and $\hat{\nu}_{2,1} = 0$.

4.1 Set-up of numerical simulations and numerical methods.

Set-up and model parametrization As introduced in Section 1, we consider a metastatic BRAF-mutated melanoma, assuming no self-seeding takes place (*i.e.* $\hat{\nu}_{2,1} = 0$), treated with Dabrafenib orally administered twice a day in the form of a 150 mg tablet (Luebker and Koepsell, 2019). To carry out numerical simulations of the system, we calibrate the model with parameters drawn from the literature. For the PK parameters we rely on the reports on Tafinlar, *i.e.* brand name for Dabrafenib, realised by the European Medicine Agency (EMA) (European Medicine Agency, 2013) and the US Food and Drug Administration (FDA) (US Food and Drug Administration, 2013), as reported in Table 1. For the parameters appearing in the cancer evolutionary dynamic model, we mainly rely on the values reported by Lorenzi et al. (2018); Villa et al. (2021). However, we set the conversion factors ψ_i $(i = 1, 2)$ in equations (12) to zero, since we consider PK parameters obtained from a model that was calibrated with *ex vivo* data and thus the value of the clearance Cl accounts for the whole process of elimination, including drug consumption by tumour cells (Balakirouchenane et al., 2020). For the migration rates we consider the ratio $\hat{\nu}_{i,j} =$ (Intravasation rate) $\times$ (Survival in the circulation) $\times$ (Extravasation probability), where the intravasation rate takes value in the range $[10^{-11}, 10^{-2}]$ cells/day (Scott et al., 2013b), the probability of survival in the circulation is in the interval $[5 \cdot 10^{-4}, 2.5 \cdot 10^{-2}]$ and the extravasation probabilities are in the range $[0.1986, 0.5461]$, as reported by Franssen et al. (2019). Building on these works, we identified upper and lower bounds that each parameter should take, selecting its reference value in this range, as detailed in Table 2.

PK parameters

Parameter	Value	Unit	Ref
k_a	1.8	h^{-1}	Balakirouchenane et al. (2020)
F	0.95	-	European Medicine Agency (2013); US Food and Drug Administration (2013); Puszkiel et al. (2019)
Cl	17	h^{-1}	Balakirouchenane et al. (2020); US Food and Drug Administration (2013)
R	0.54	h^{-1}	European Medicine Agency (2013); US Food and Drug Administration (2013)
V_c	37.525	l	Balakirouchenane et al. (2020); Puszkiel et al. (2019)
V_b	5	l	Sharma and Sharma (2022)
$k_{in,p}$	0.0974	h^{-1}	Balakirouchenane et al. (2020)
$k_{out,p}$	0.196	h^{-1}	Balakirouchenane et al. (2020)

Table 1: Pharmacokinetics parameter values.

Tumour site specific parameters

Parameter	LB	UB	RV $i=1$	RV $i=2$	Unit	Ref
Q_i	-	-	0.3	0.01	lh^{-1}	Jones and Rowland-Yeo (2013)
V_i	-	-	0.5	0.05	l	Gallo et al. (2004)
K_i	-	-	0.8	0.5	-	Mittapalli et al. (2013)
β_i	10^{-13}	10^{-8}	10^{-9}	10^{-9}	s^{-1}	Chisholm et al. (2015)
δ_i	10^{-5}	10^{-3}	10^{-4}	10^{-4}	s^{-1}	Ward and King (1997)
φ_i	10^{-7}	10^{-5}	10^{-5}	10^{-5}	s^{-1}	Gordan et al. (2007)
η_i	10^{-5}	10^{-3}	$1.8\cdot10^{-4}$	$1.8\cdot10^{-4}$	s^{-1}	Ward and King (1997)
α_i	10^{-7}	10^{-5}	$2\cdot10^{-6}$	$2\cdot10^{-6}$	g cm^{-3}	Norris et al. (2006)
d_i	10^{-14}	10^{-12}	$2\cdot10^{-13}$	$2\cdot10^{-13}$	cm^3 s^{-1} $cells^{-1}$	Li (1982)
$\hat{\nu}_{i,j}$	10^{-12}	10^{-8}	$1.3\cdot10^{-10}$	0	s^{-1}	Franssen et al. (2019); Scott et al. (2013b)

Table 2: Parameter lower bounds (LB), upper bounds (UB) and reference values (RV), for the primary tumour site ($i=1$) and its metastasis ($i=2$).

Numerical methods Numerical solutions are constructed using a uniform discretisation of the interval $[0,1]$, consisting of 101 grid points, as the computational domain of the independent variable y. We consider $t\in[0,T]$, with $T>0$ being the final time of simulations, chosen sufficiently large to reach steady state or to mimic the duration of therapy. We discretize the interval $[0,T]$ with a uniform step, sufficiently small to ensure numerical stability under each parameter set used. We construct numerical solutions employing an explicit scheme, based on a first order forward difference approximation in time and a second order central difference approximation in space, applied also to the zero-flux boundary conditions. Following Almeida et al. (2019); Villa et al. (2021), we set the initial phenotypic distribution in each site $n_{i,0}(y)$ to be a weighted normal distribution, centered in 0 and truncated in $[0,1]$, integrating to the initial cell density $I_{i,0}$, *i.e.*

$$n_{i,0}(y)=\frac{I_{i,0}}{\Theta}\exp\left(-\frac{y^2}{8\cdot10^{-6}}\right),\quad\text{with}\quad\Theta=\int_0^1\exp\left(-\frac{y^2}{8\cdot10^{-6}}\right)dy\,.$$

We chose this consistently with the assumption that most cancer cells are sensitive to the drug prior to treatment, and we also set as initial population size $I_{i,0}=\frac{\delta_i}{d_i}$. All numerical computations are performed in MATLAB.

Steady-state criterion We denote by T_{ss} the time at which the solution of an equation reaches numerical equilibrium, in particular we study this quantity for each of the phenotypic distributions $n_i(t,y)$. In order to identify this numerically, we consider a sufficiently small tolerance, $tol>0$, below which the relative difference in the numerical solution at two consecutive time steps is considered to no longer be significant. Let $n_{i,j}^k$ denote the numerical approximation of the density of cancer cells in site i ($i=1,2$), endowed with

phenotypic trait y_j ($j = 0, \dots, J$), at time step t_k ($k = 0, \dots, N$). Then, we define the relative difference $D_{i,k}$ between the phenotypic distribution at site i at two consecutive time steps t_{k-1} and t_k as:

$$D_{i,k} = \frac{1}{J+1} \sum_{j=0}^{J} \left| \frac{n_{i,j}^k - n_{i,j}^{k-1}}{n_{i,j}^k} \right| \quad \text{for} \quad 1 \leq k \leq N \,, \tag{35}$$

and denote T_{ss} as the first time step t_k after which the inequality $D_{i,k} < tol$ is always satisfied for $i = 1, 2$.

4.2 Global sensitivity analysis

We here make use of Global sensibility analysis (GSA) to verify that the insights gained from the analytical results of Section 3 still hold outside the asymptotic regime of rare spontaneous phenotypic changes. GSA is the study of how uncertainty in the output of a model can be apportioned to different sources of uncertainty in the model input and, specifically, it offers a wide overview of how the parameter interactions impact the model output. The most suitable GSA techniques for systems modelling highly non-linear dynamics, generally the case in biological applications and certainly the case in this work, are the elementary effect (EE) and Sobol methods (Kiparissides et al., 2009; Qian and Mahdi, 2020).

EE method The EE method is of screening type, *i.e.* it aims at identifying the parameters that have negligible impact on the output variability, and is intended for use when dealing with a large number of input parameters, since it has a lower computational cost w.r.t. other methods. Inspired by the *radial design* strategy proposed by Campolongo et al. (2011), we consider a vector Z of p independent input parameters Z_i ($i = 1, ..., p$), varying in their input space. Given the model output $Y = f(Z)$, we compute r evaluations of the elementary effect EE_i^l ($l = 1, ..., r$) associated to the i-th input factor. Given two sample points of Z, *e.g.* $a^l = (a_1^l, \dots, a_p^l)$ and $b^l = (b_1^l, \dots, b_p^l)$, the elementary effect EE_i^l is defined as

$$EE_i^l = \frac{f((a_1^l, \dots, a_i^l, \dots, a_p^l)) - f((a_1^l, \dots, b_i^l, \dots, a_p^l))}{a_i^l - b_i^l} \,, \quad l = 1, ..., r \,. \tag{36}$$

We also compute the corresponding measures as

$$\overline{EE}_i = \frac{1}{r} \sum_{l=1}^{r} EE_i^l \,, \quad \overline{EE}_i^* = \frac{1}{r} \sum_{l=1}^{r} |EE_i^l| \quad \text{and} \quad SD_i = \left(\frac{1}{r} \sum_{l=1}^{r} (EE_i^l - \overline{EE}_i)^2 \right)^{1/2} . \tag{37}$$

In particular:

- $\overline{EE}_i$ (*sensitivity measure*) represents the overall influence of the i-th parameter on the output. $\overline{EE}_i^*$ has the same meaning but is adopted for avoiding the cancellation effect when dealing with non-monotonic models.
- SD_i (*interactions measure*) gives information of the non-linearity and/or interaction effects of the i-th input. If it is small it means that the EE_i are similar all along the sample space, suggesting a linear relationship between the i-th input and the output. On the contrary, if it is large it means that the EE_i are strongly affected by the sample point at which they are computed, thus the parameter effects are considered to be non-linear and/or due to interaction with other factors.

Sobol method The Sobol method is a variance-based technique, and is both of screening and ranking type, *i.e.* it aims at ordering the inputs based on their impact on the output variability. This approach is computationally demanding, since it requires a large number of model simulations. For this reason, it is usually adopted for a small set of input parameters. Given the input vector Z and the model output Y, the Sobol indices are given by

$$S_i = \frac{Var(\mathbb{E}[Y|Z_i])}{Var(Y)}, \quad \text{and} \quad S_{Ti} = S_i + \sum_{u \subseteq \{1,\dots,p\} \setminus \{i\}} \frac{Var(\mathbb{E}[Y|Z_i, Z_u])}{Var(Y)} \,, \tag{38}$$

which are both non-negative. In particular:

- S_i provides the first-order contribution of the i-th input to the output variance and measures the main effect of Z_i.

- S_{Ti} measures the total effect of the parameter Z_i on the output. $S_{Ti} = 0$ implies that the parameter Z_i is non-influential, while a significant difference between S_i and S_{Ti} suggests that the factor Z_i is involved in important interactions.

We compute the primary and total indices adopting the Monte Carlo method, and in particular we make use of the estimators for S_i and S_{Ti} suggested by Saltelli (2002).

Model inputs and outputs We consider $Z = (\beta_1, \beta_2, \varphi_1, \varphi_2, \delta_1, \delta_2, \alpha_1, \alpha_2, \eta_1, \eta_2, d_1, d_2, \hat{\nu}_{1,2})$ and the input vector of the GSA, while the other parameters are fixed to the reference values of Tables 1 and 2. We consider each parameter a random variable, independent from the others, distributed with a log-uniform distribution in the ranges defined in Table 2. We adopt this distribution in order to better explore the different orders of magnitude of the input parameters. Furthermore, we take into account a drug schedule of 150 mg oral tablets twice a day, and set a final time $T = 91$ days. We consider two model outputs:

- $Y_I = I_1(T) + I_2(T)$, *i.e.* the total tumour mass at time T;
- $Y_\mu = \frac{\mu_1(T)+\mu_2(T)}{2}$, *i.e.* the mean phenotypic trait average between the two tumour sites at time T.

We have used Sobol' quasi-random sequences in order to generate our sets of quasi-random points (Campolongo et al., 2011).

4.2.1 Results of the EE method for GSA

Figure 4 displays the results of EE method for GSA, from which we remark the following:

1) Figures 4a.3 and 4b.3 display the ratios between SD and $\overline{EE}^*$ for the two model outputs. They both display non-linearity and/or interactions between the parameters, consistently with the non-linear nature of the model. In particular, for both outputs the migration rate $\hat{\nu}_{1,2}$ seems to have a highly non-linear effect and/or to strongly interact with the other factors, consistently with its key role in connecting the dynamics in the two sites.

2) For Y_I the indices $\overline{EE}^*$ and $\overline{EE}$ are in agreement (Figures 4a.2 and 4a.1), indicating a lack of cancellation effects and thus a monotonic nature of the input-output response. This is not the case for Y_μ (Figures 4b.2 and 4b.1) for which many parameters show both negative and positive EE_i, suggesting a non-monotonic behaviour.

3) Consistently with the analytical results of Section 3.3, in Figure 4a.2 we can observe that parameters δ_i, d_i and η_i $(i = 1, 2)$ have the largest impact on the total cell number Y_I. Figure 4a.1 shows that the EE_i evaluations for d_i and η_i are negative, while those for δ_i are positive, in agreement with equations (8) and (34).

4) In Figure 4b.2 we can observe that parameters δ_i, β_i, and η_i $(i = 1, 2)$ exhibit the largest impact on the mean phenotypic trait average Y_μ, which is consistent with the analytical results of Section 3.3. In particular, in Figure 4b.1 we observe that most of the EE_i evaluations for η_i are positive, in agreement with equations (8) and (33) in which y_i is proportional to the maximum cytotoxic death rate.

5) It is interesting to notice that β_i $(i = 1, 2)$ emerge as significant input parameters for Y_μ, with their EE_i evaluations being all positive (cf. Figure 4b.1). This finding, which could not emerge from the analytical results due to the asymptotic regime considered in Section 3, reasons with the fact that higher values of β_i should correlate with a larger variance of the phenotypic distributions – *e.g.* as seen in (Villa et al., 2021) – which may shift the mean of the distribution in the bounded domain $[0, 1]$.

6) We note that the migration rate $\hat{\nu}_{1,2}$ has negligible impact on both outputs, likely due to the small value it may take in the admissible range for the GSA. Considering a wider range of values, *i.e.* $\hat{\nu}_{1,2} \in [10^{-12}, 10^{-5}]$, we observed an increase in the importance of this parameter, as expected, particularly for Y_μ (cf. Figure S.4). Nonetheless, a highly non-linear effect is still observed in both parameter ranges.

7) The Michaelis-Menten coefficients α_i $(i = 1, 2)$ exhibit a really low impact on both outputs, likely due to the large dose of drug injected. In fact, considering a lower drug dose leads to an increase in the

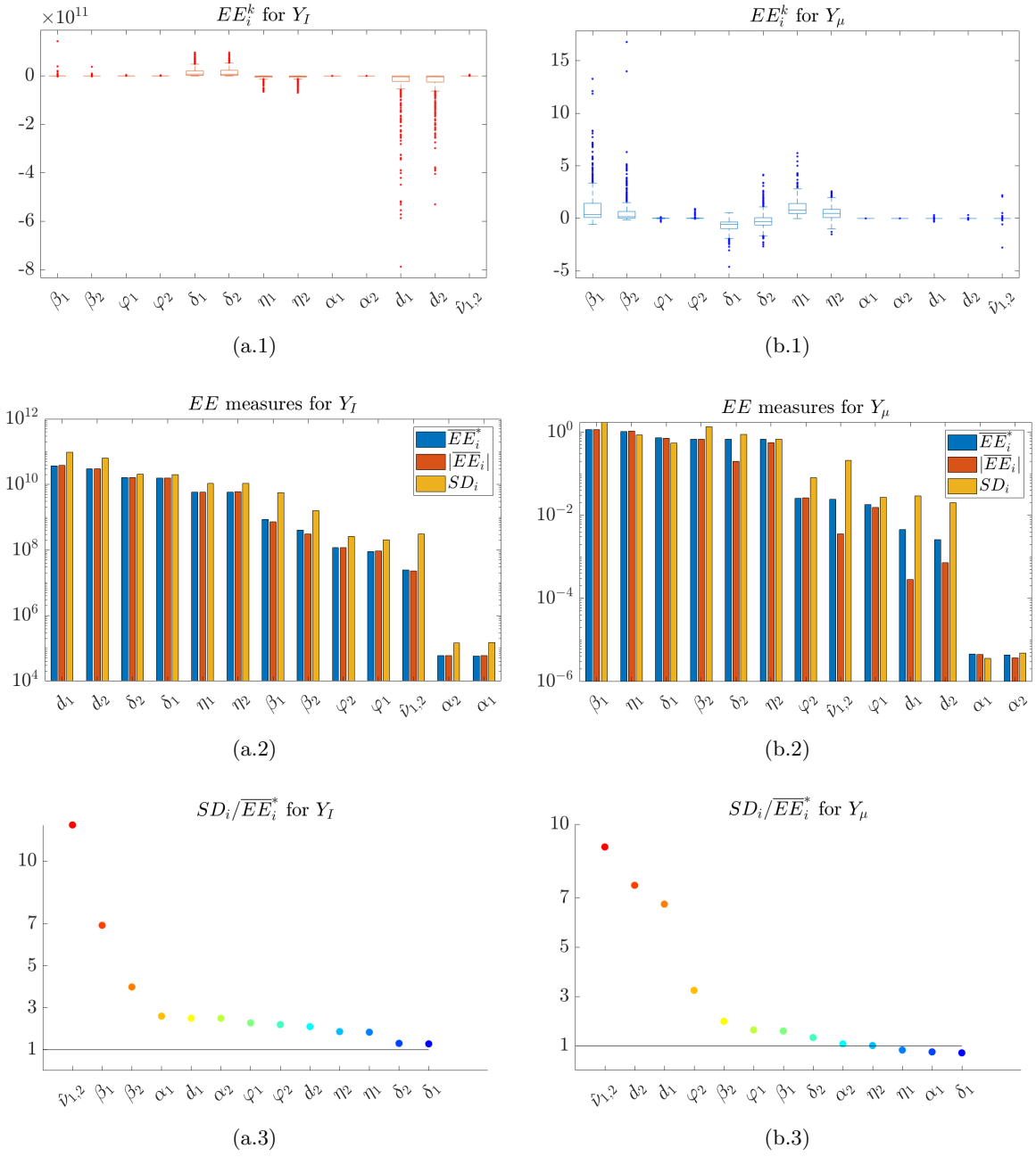

Figure 4: **Results of the Elementary effects method for GSA.** EE measures associated with the model output Y_I (a.1-3) and Y_μ (b.1-3), *i.e.* the total tumour mass and average mean phenotypic state of the sites. The estimates are computed with $r = 500$ evaluations of the elementary effect for each parameter. The elementary effects EE_i, defined in (36), calculated for each parameter are displayed in plots (a.1) and (b.1). The associated measures $\overline{EE}_i^*$, $|\overline{EE}_i^*|$ and SD_i, defined in (37), are shown in plots (a.2) and (b.2). Plots (a.3) and (b.3) present the ratio between SD and $\overline{EE}_i^*$.

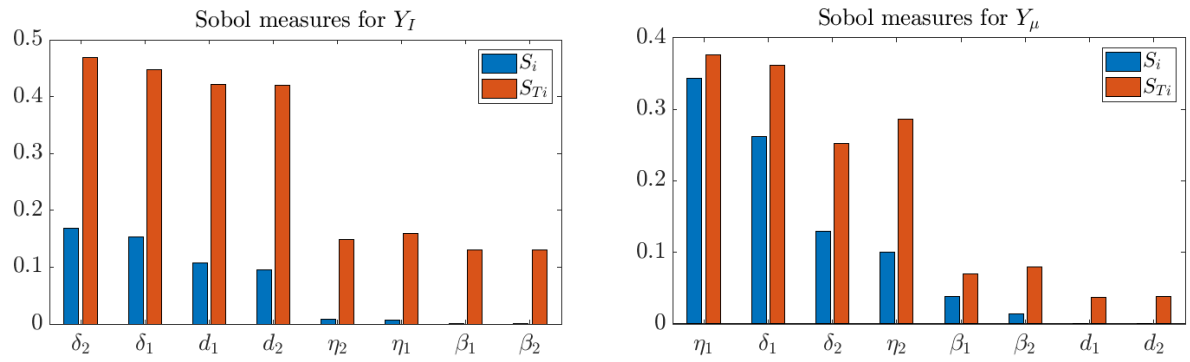

(a) (b)

Figure 5: **Results of the Sobol method for GSA.** Sobol measures S_i and S_{Ti}, defined in (38), associated with the model output Y_I (a) and Y_μ (b), *i.e.* the total tumour mass and average mean phenotypic state of the sites. The estimates are computed from 5000 sample points in the input space.

importance of α_i, along with a decrease in the importance of the maximum death rate η_i (cf. Figure S.5). This suggests that at low drug doses, increasing the cytotoxic efficiency of the compound will not yield significant therapeutic improvements.

4.2.2 Results of Sobol method for GSA

We conduct further GSA following the Sobol strategy on the most influential parameters highlighted by the results obtained with the EE method. We thus consider a shorter input vector $Z = (\beta_1, \beta_2, \delta_1, \delta_2, \eta_1, \eta_2, d_1, d_2)$ and fix the rest of the parameters to the reference values of Table 2. The obtained results, illustrated in Figure 5, are generally consistent with the findings of the GSA following the EE method. In addition, several notable observations can be made:

8) In contrast to the results obtained from the EE method, β_i $(i = 1, 2)$ appear to have relatively low importance for Y_μ. Moreover their S_{Ti} are significantly bigger than the S_i, implying that they mainly act in interaction with the other parameters. This suggests that higher rates of phenotypic changes, and thus intra-population heterogeneity, imply greater complexity and non-linearity.

9) Parameters associated with the primary tumour exhibit higher values of S_i. This may be due to the fact that we consider a metastatic spread scenario, where the primary tumour affects the metastasis, but not the other way around.

10) For Y_I, the significantly higher values of S_{Ti} compared to those of S_i provide further evidence of the importance of interactions among these parameters. Meanwhile, for Y_μ the S_i values occupy a considerable proportion of S_{Ti}, showing that the main effects of η_i and δ_i are more important than their interactions.

4.3 Numerical simulations

Given the findings of the GSA, we further explore how the most impactful parameters affect the model outcome. Specifically, we investigate how different tumour environments may influence possible treatment outcomes, and how different factors or biological processes may influence the evolutionary timeline of the tumours under treatment.

4.3.1 Highly communicating sites with different tissue-to-plasma partition coefficients

In this section we take into account two different scenarios, referred to as the baseline and non-baseline scenarios, which take different values of the maximum migration rate $\hat{\nu}_{1,2}$ and the partition coefficients of the two sites K_i $(i = 1, 2)$, as summarised in Table 3. Specifically, the non-baseline one is an extreme scenario in which we significantly increase the migration rate from primary tumour to the metastasis to a

	Baseline scenario		**Non-baseline scenario**			
Parameter	$i=1$	$i=2$	$i=1$	$i=2$	Unit	Ref
K_i	0.8	0.5	1	10^{-4}	-	Mittapalli et al. (2013)
$\hat{\nu}_{i,j}$	$1.3 \cdot 10^{-10}$	0	$1.3 \cdot 10^{-5}$	0	s^{-1}	Franssen et al. (2019); Scott et al. (2013b)

Table 3: Cancer physiological and evolutionary dynamics parameter values for the baseline and non-baseline scenarios. K_i represents the partition coefficient of site i, and $\hat{\nu}_{i,j}$ the maximum migration rate from site i to site j, where $i=1$ is the primary tumour and $i=2$ the metastatic site.

value out of the range reported in Table 2. We do this for illustrative purposes, as from the results of the GSA we expect to be able to more easily observe the potential impact of the communication between sites by considering parameter values outside this range. In addition, we vary the partition coefficients of the tissues in the two sites, in order to consider how significantly different tumour environments in different sites may affect the treatment outcome in metastatic tumours. In fact, the parameter K_i indicates the degree of tissue drug accumulation, attributed to phenomena such as protein binding, lysosomal trapping, and lipid dissolution (Jones and Rowland-Yeo, 2013), and a smaller value of K_2 compared to that of K_1 implies a lower drug concentration will accumulate in the metastatic site compared to the primary. In order to mainly focus on the impact of these biological factors on the treatment outcome, the other parameters are fixed to their reference values of Tables 1 and 2, and are thus the same in both scenarios.

Different *in situ* drug concentrations Figure 6 displays the drug concentration in four compartments, excluding the administration site for visualisation purposes. First of all, we remark that the peak of the plasma compound concentration (C_c) is reached at the time $t_{max} = 0.93$ h, and with a value of $C_{c,max} = 0.0022$ g/l, of the same order of magnitude of the values found in literature (European Medicine Agency, 2013; US Food and Drug Administration, 2013). Moreover, the drug concentration in the metastatic site (C_2) is significantly lower in the non-baseline scenario compared to the baseline one, reaching a maximum value of the order of 10^{-7} g/l while in the baseline scenario it reaches higher peaks comparable to those reached by the drug concentration in the primary site (C_1). This is consistent with the biological meaning of K_i, and highlights how different tissue-to-plasma partition coefficients may result in different drug concentrations in the two tumour sites, creating substantial discrepancies between the two tumour environments.

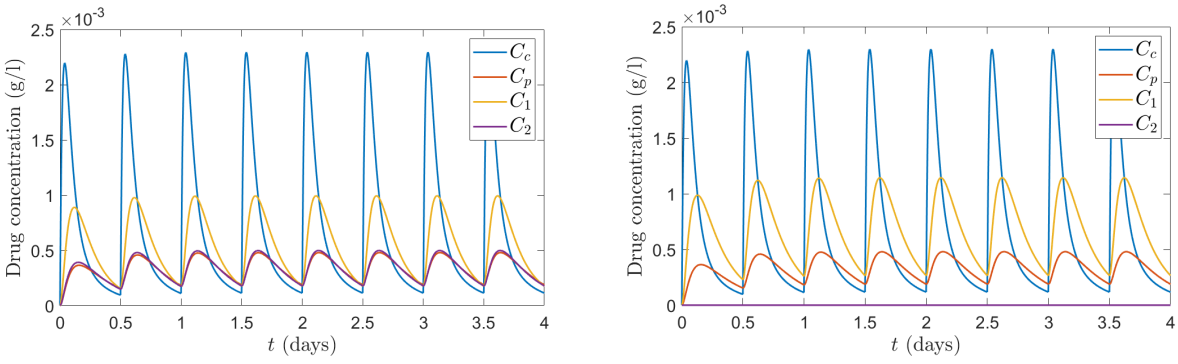

(a) Baseline scenario.

(b) Non-baseline scenario.

Figure 6: **Drug concentrations under baseline and non-baseline scenarios.** Pharmacokinetics results of the numerical simulations under the baseline (a) and non-baseline (b) scenarios with the drug schedule of 150 mg orally administered twice a day, and a final time $T = 4$ days. For each scenario we plot the drug concentration in the central (blue), peripheral (orange), primary tumour (yellow) and metastatic tumour (purple) compartments. More details on the simulation set-up and numerical methods can be found in Section 4.1.

Different evolutionary outcomes of the tumours Such a difference in drug concentration in the two sites in the non-baseline scenario results in different evolutionary dynamics of the two tumour populations, unlike in the baseline scenario where no significant difference is observed between the phenotypic distributions in the two sites, as illustrated in Figure 7 comparing the long-term evolution of the tumour populations in the two scenarios. In particular, in the non-baseline scenario we observe that the lower drug concentration accumulating in the metastatic site results in a population mostly characterised by lower levels of drug resistance compared to that in the primary site, exposed to a higher compound concentration. Nonetheless, the high migration rate results in a small subpopulation in the metastatic site presenting levels of resistance comparable to those developed in the primary tumour. In the baseline scenario, cell migration has no meaningful impact on the phenotypic distribution given the similarity of the tumour environments, consistently with the analytical results illustrated in Figure 3 (second column).

Consistency with analytical results The obtained results are consistent with the analytical study of Section 3. In fact, from definitions (8), by significantly decreasing C_2 we obtain a lower fittest phenotypic trait h_2 and selective gradient b_2, and a higher maximum fitness a_2. Following (33), this results in a lower selected trait y_2 and a higher metastatic population size I_2, which is exactly what we detect in Figure 7. Given the considerably different selected traits in the two sites, *i.e.* y_1 and y_2, and the increased migration rate, the population of the metastatic site shows polymorphism, in accord with equations (32) and (34). Moreover, we detect a slight decrease in both the primary tumour population size and selected trait, in agreement with equation (34) considering that the order of magnitude of the migration rate is lower than that of b_1.

Sensitivity of cancer evolutionary dynamics to temporal oscillations in drug concentrations Indeed temporal oscillations in the *in situ* compound concentration, due to the drug administration schedule, imply temporal oscillations in the moments of the phenotypic distribution during treatment, as can be better observed by plotting the solutions of Figure 7 over just two days (cf. Figure S.6). As already clear from Figure 7, the great variability of the I_2 curve in the non-baseline scenario indicated that the metastatic population size is considerably susceptible to the drug concentration variation. In fact, it can be detected from the zoomed-in plots that under both scenarios I_i is the most sensitive to the drug concentration variations, while both μ_i and σ_i^2 are substantially less susceptible. This may be explained by noticing that while the pharmacokinetics are in the scale of hours, the cancer evolutionary dynamics, *i.e.* the phenotypic adaptation of the cancer cell populations to the local environments, are in the scale of days. Nonetheless, we remark that the fluctuations of these quantities are negligible in the baseline scenario and in the primary site of the non-baseline scenario, where their amplitude is small compared to the average value of the respective quantity. This is not as much the case in the metastatic site of the non-baseline scenario, characterised by a lower average drug concentration and thus higher sensitivity to small variations of this quantity. We thus conclude that a higher administered drug dose may result in a lower evolutionary dynamics sensibility to the compound variability.

4.3.2 Oral administration vs intravenous injection

In the previous section we remarked that under the drug administration regimen of a 150 mg oral dose twice a day, in the baseline scenario, the impact of the drug concentration oscillations on the evolutionary dynamics and overall therapeutic outcome is negligible. We thus wish to conduct further numerical investigations considering the equilibrium phenotypic distribution to which the system converges at the end of treatment, as well as the time it takes to reach this. However, considering oral drug administration the system does not reach numerical steadiness for either scenario, as can be seen from the lower-right panels of Figure 7 displaying the step-difference $D_{i,k}$ introduced in equation (35), which becomes approximately periodic with a 12 h period (cf. zoom-in plot in Figure S.6), *i.e.* the time interval between two consecutive drug administrations. This would not be the case if we considered a constant intravenous drug injection.

Therefore, we aim at finding the intravenously-injected constant drug dose leading to cancer evolutionary dynamics analogous to those obtained with an orally-administered drug dose of 150 mg twice a day for $T = 105$ days, which we will use in the next section for convenience, acknowledging that Dabrafenib is administered *per os* to patients. Given the final distribution obtained with the dose administered twice a day $n_i^*(T)$ and the final distribution obtained with a constant intravenously-injected dose $n_i^{dose}(T)$, we define

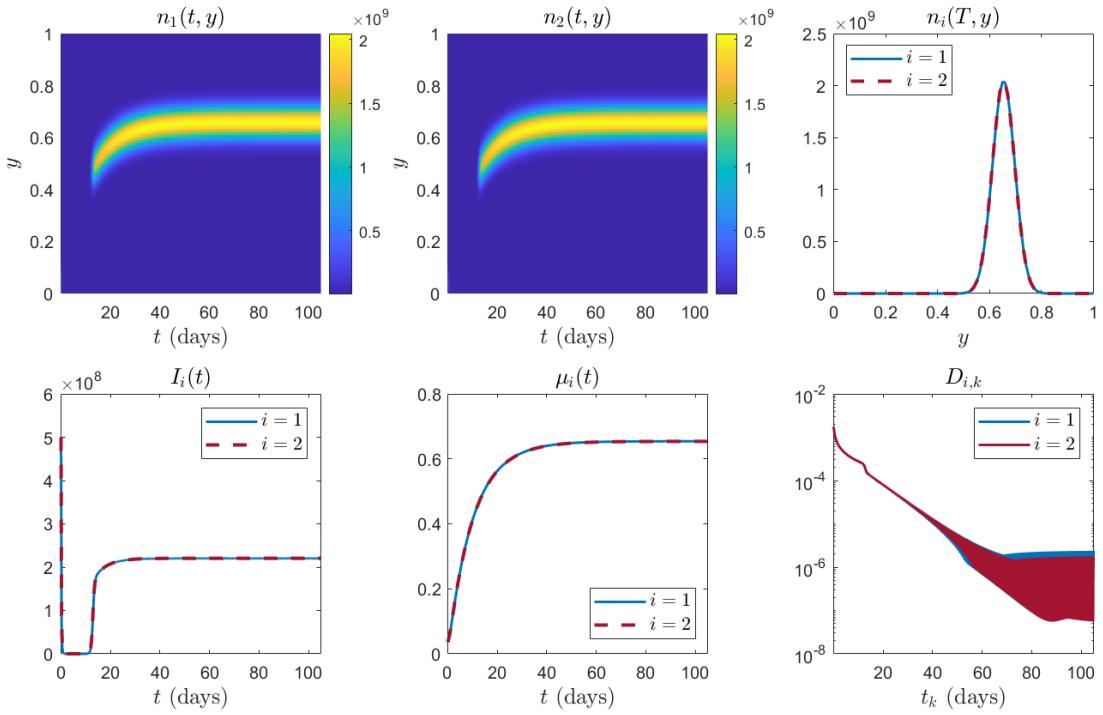

(a) Baseline scenario

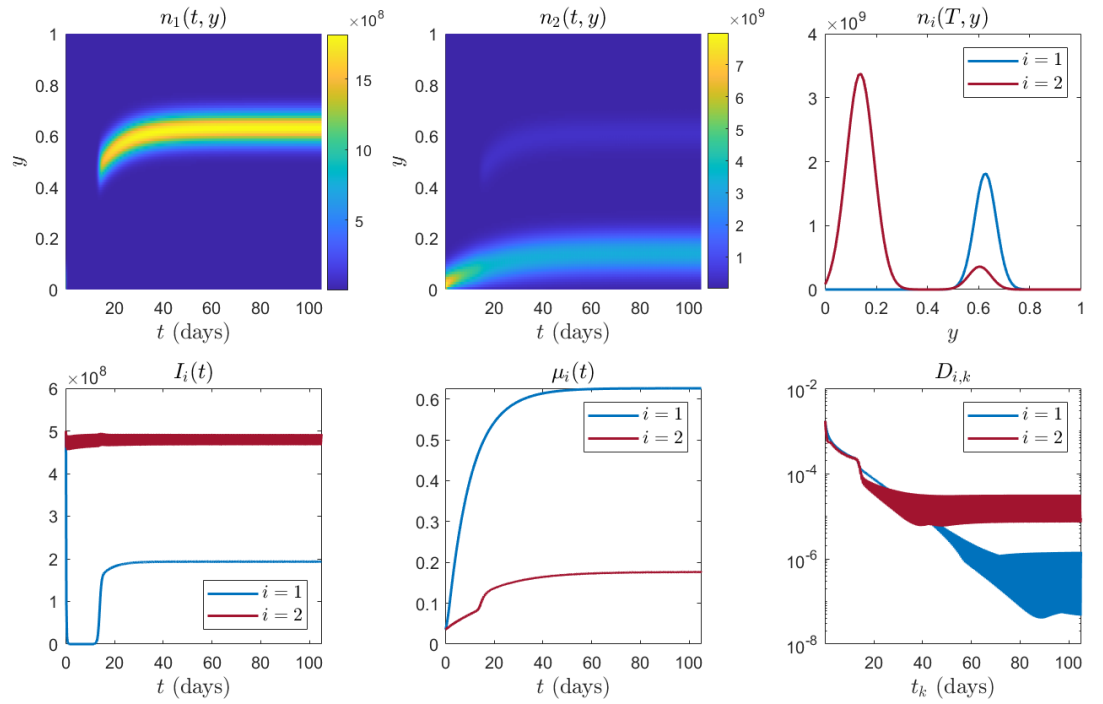

(b) Non-baseline scenario

Figure 7: **Cancer evolutionary dynamics under baseline and non-baseline scenarios.** Cancer evolutionary dynamics results of the numerical simulations under the baseline (a) and non-baseline (b) scenarios with the drug schedule of 150 mg orally administered twice a day, and a final time $T = 105$ days. For each scenario we plot in the first row the phenotypic distribution over time of the primary tumour $n_1(t, y)$ (first panel) and the metastatic tumour $n_2(t, y)$ (second panel), and compare them at the final time T, *i.e.* $n_i(T, y)$, (third panel), and we plot in the second row the population sizes $I_i(t)$ (first panel), mean phenotypic traits $\mu_i(t)$ (second panel) and step differences $D_{i,k}$ (third panel), as respectively defined in equations (1), (2) and (35). More details on the simulation set-up and numerical methods can be found in Section 4.1.

the relative error between the two outcomes as

$$err_{i,dose} = \frac{1}{J}\sum_{j=1}^{J}\left|\frac{n^*_{i,j}(T) - n^{dose}_{i,j}(T)}{n^*_{i,j}(T)}\right|. \tag{39}$$

Minimising the function $f(dose) = 0.5\,(err_{1,dose} + err_{2,dose})$ in the baseline scenario, we obtain that the intravenously-injected drug dose that best reproduces the evolutionary outcomes of the oral administration regimen is of 2.6915 μg/s. We verified that this optimal dose also provides a good approximation of the dynamics obtained in the non-baseline scenario, as displayed in Figure 8. Moreover, we report the times T_{ss} at which the phenotypic distributions in the two sites reach steadiness, which are larger than the median time of response and below the median Dabrafenib treatment durations reported in (Martin-Algarra et al., 2019).

	T_{ss} of n_1	T_{ss} of n_2
Baseline	66.98 days	67.02 days
Non-baseline	65.24 days	59.16 days

Table 4: Steady state time of the phenotypic distribution of the primary tumour (T_{ss} of n_1) and the metastasis (T_{ss} of n_2) in the baseline and non-baseline scenarios under an intravenously-injected constant drug dose of 2.6915 μg/s. The steady state time is the first time at which $D_{i,k} < tol$, with $D_{i,k}$ defined in (35) and a tolerance of $tol = 10^{-6}$.

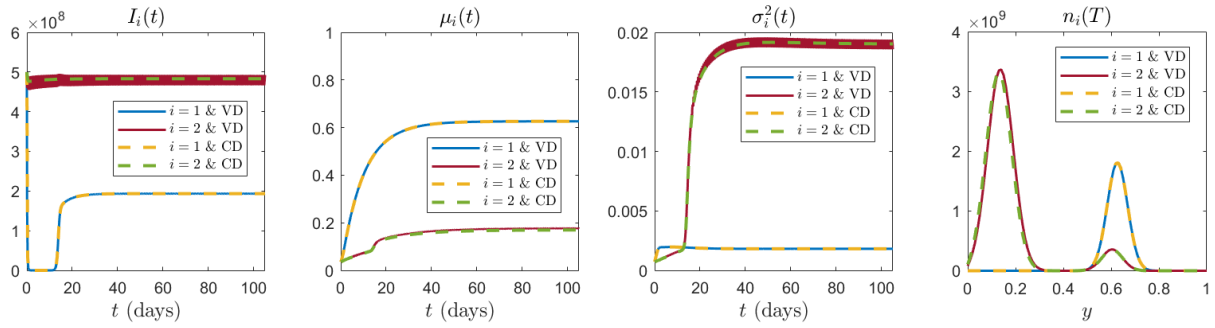

Figure 8: **Oral administration vs intravenous injection under non-baseline scenario.** Cancer evolutionary dynamics results under the non-baseline scenario and a drug schedule of 150 mg orally administered twice a day (VD) or constant intravenous injection of 2.6915 μg/s (CD), and final time $T = 105$ days. From left to right, the panels display the cancer population sizes $I_i(t)$, the mean phenotypic traits $\mu_i(t)$ and the corresponding variances $\sigma_i^2(t)$ over time for the two tumour cell populations, respectively defined in equations (1), and (2), and the phenotypic distributions at time T, *i.e.* $n_i(T, y)$. More details on the simulation set-up and numerical methods can be found in Section 4.1.

4.3.3 Steady-state study of treatment outcomes

Having identified the dose of constant intravenous drug injection that yields analogous therapeutic outcomes to the oral administration regimen used in the clinic, we now investigate how the therapeutic outcome may be affected by some key factors. Specifically, we consider the level of vascularisation of the metastatic tumour, *i.e.* a physiological factor which will regulate the distribution of the compound in the metastatic site, and the most important parameters emerged from the GSA focussing on Y_μ as the model output , *i.e.* δ_i, η_i ($i = 1, 2$) and β_i. This choice is motivated by the fact that the mean phenotypic trait μ_i in the two tumours gives us an indication of the development of drug resistance during treatment. Moreover, as highlighted in the previous section, μ_i is the least affected by the drug concentration variability, and we thus expect conclusions drawn in this section to hold in both drug delivery regimens with higher certainty. We also remark that from the analytical results of Section 3 we expect that the total population in the sites (I_i) depends on the selected traits (y_1 and y_2), but not viceversa.

To test the influence of these factors on the treatment outcome, for each parameter we vary its value in the range defined in Table 2, and compare the model outputs, *i.e.* the cancer population sizes I_i and mean phenotypic traits μ_i in the two sites, after 30 weeks of continuous intravenous constant drug administration, *i.e.* the average length of Dabrafenib treatment (Martin-Algarra et al., 2019). For each simulation we also report on when the drug concentration and the phenotypic distributions in the two sites reach steady state, as it gives insights in how the different input factors affect the speed of the cancer cell adaptation to the drug regimen. This also suggests reasonable timeframes in which to assess the advancement of the therapeutic intervention.

Fitness-related parameters Figure 9a and Figure 9b display the model sensitivity to the maximum background fitness for highly proliferating yet sensitive cells, δ_i $(i = 1, 2)$, and the maximal death rate of sensitive cells, η_i $(i = 1, 2)$, respectively. We notice that incrementing δ_i speeds up the adaptive dynamics, increases the cancer cell population sizes, while decreasing the mean phenotypic traits. Meanwhile, consistently with its biological meaning, we detect that incrementing η_i decreases the cancer cell population sizes, while increasing the mean phenotypic traits, but has no consistent impact on the adaptation speed. All these findings are in line with previous analytical results in the literature (Almeida et al., 2019; Villa et al., 2021).

Epimutation rate Since the effects of the epimutation rates β_i $(i = 1, 2)$ could not emerge from the asymptotic analysis of Section 3, and the results of the GSA yield contrasting information on the importance of these parameters, we consider the results of the numerical steady-state investigation, reported in Figure 9c. We immediately notice that as β_i take greater values the phenotypic distributions n_i reach steadiness faster, implying a greater speed of adaptation. On the other hand, in the parameter range considered, β_i do not appear to affect I_i and μ_i, as suggested by the results of the Sobol method for GSA, although increasing the epimutation rates results in a higher variance of the phenotypic distribution (cf. Figure S.7), resulting in a more heterogeneous population. These findings are consistent with analytical results in the literature (Almeida et al., 2019; Villa et al., 2021), highlighting that higher epimutation rates increase phenotypic diversity, in turn speeding up natural selection.

Vascularisation of the metastatic site Lastly, we study the effect of the level of vascularization of the metastatic site on the evolutionary timeline during treatment by varying the blood flow-to-volume ratio, *i.e.* Q_2/V_2. From Figure 10 it is evident that a lower blood flow-to-volume ratio delays the time at which the *in situ* compound concentration reaches its equilibrium value. This can be seen in Figure 10a for C_2 compared to the drug concentration in the other model compartments, and it is consistent with the biological interpretation of these factors: given that there is less blood entering the metastatic site, and consequently less compound, it takes much more time for the tissue to fill up. We remark that for $Q_2/V_2 \geq 2 \cdot 10^{-2}$ 1/h, *i.e.* for particularly well vascularised metastatic tumours, the steady-state time of the local phenotypic distribution remains constant, as can be observed in Figure 10b. Nonetheless, for lower values of the ratio Q_2/V_2 we observe that the steady-state time for n_2 significantly increases, indicating that for particularly low levels of tumour vascularisation the slower drug perfusion delays the cancer evolutionary dynamics.

5 Conclusions

5.1 Summary of major results

In this paper, we conducted a mathematical study of the evolutionary dynamics of metastatic tumours under chemotherapy. Specifically, our approach involves formal asymptotic analysis and numerical simulations of a system of non-local PDEs describing the phenotypic evolution of the tumour cells coupled with a system of ODEs modelling the cytotoxic drug pharmacokinetics.

Focusing on a biological scenario allowing for metastatic spread but no secondary or self-seeding, the analytical results indicate that, while the primary tumour will evolve into a monomorphic population with trait selected according to local environmental conditions, the metastasis may display polymorphism if local environmental conditions differ from those in the primary site, with a subpopulation of cells presenting traits selected in the primary tumour. Moreover, the size of this subpopulation increases as the connectivity of the sites and the migratory ability of cells selected in the primary tumour increases, or as the selective pressure in the metastatic site decreases.

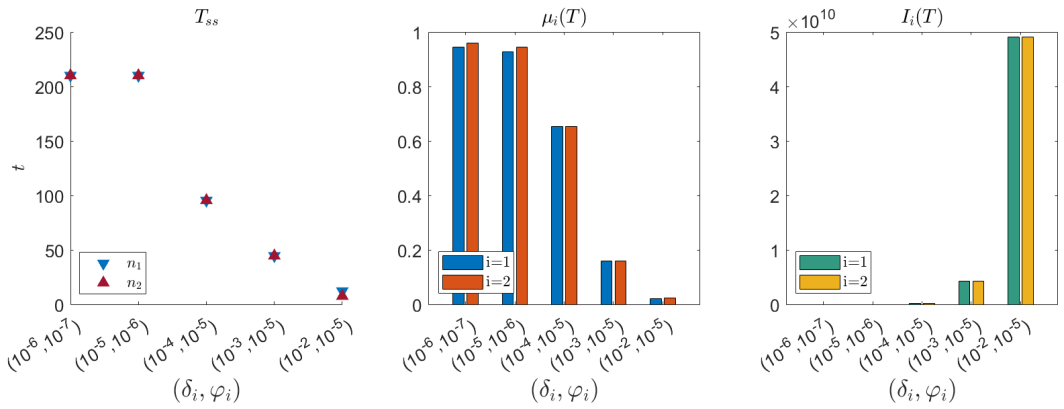

(a) Maximal background fitness

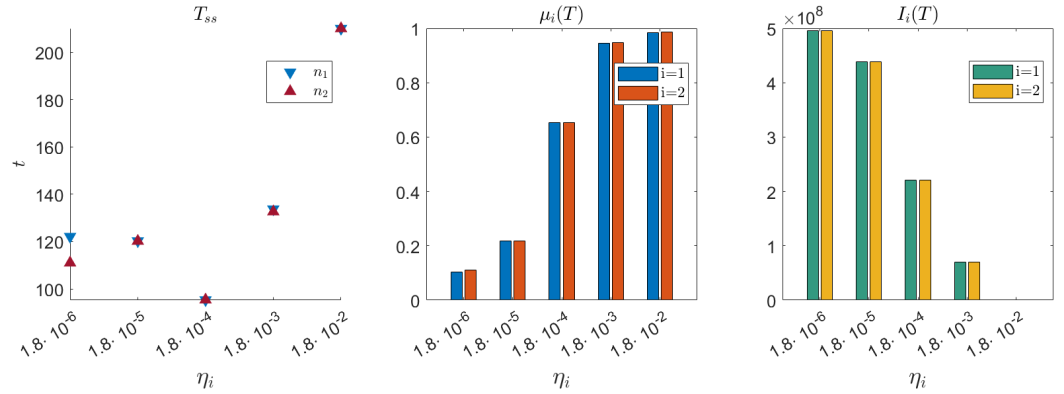

(b) Maximum cytotoxic death rate

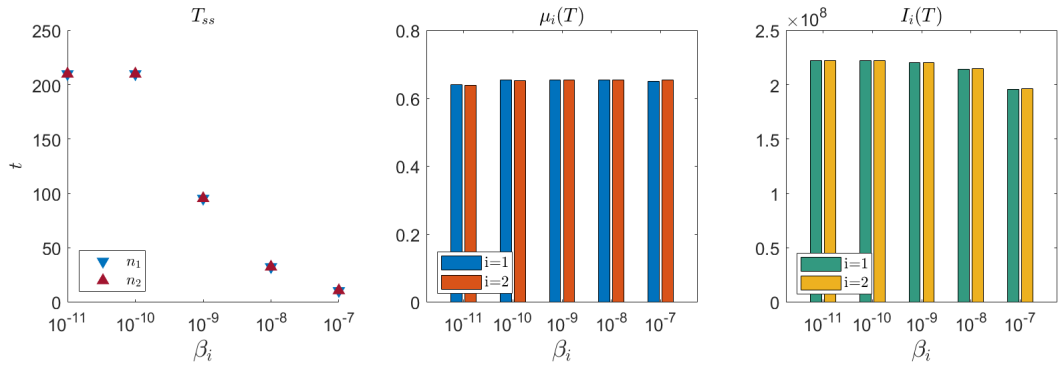

(c) Epimutation rate

Figure 9: **Treatment outcome dependency on δ_i, η_i and β_i.** Treatment outcomes obtained from numerical simulations of the model under the baseline scenario, for an intravenously-injected drug dose of 2.6915 μg/s and a final time of $T = 210$ days. The graphs display the steady-state times (first panel), mean phenotypic traits (second panel) and tumour sizes (third panel) at steady state, varying: a) the maximal background fitness δ_i, and φ_i to ensure the assumption $\delta_i \gg \varphi_i$ still holds; b) the maximum cytotoxic death rate η_i; c) the epimutation rate β_i. The steady state time is the first time at which $D_{i,k} < tol$, with $D_{i,k}$ defined in (35) and a tolerance of $tol = 10^{-6}$. More details on the simulation set-up and numerical methods can be found in Section 4.1.

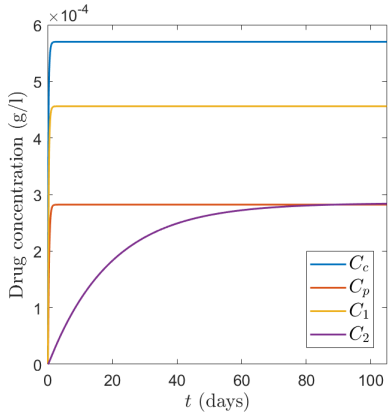

(a) Drug concentrations for $Q_2/V_2 = 2 \cdot 10^{-3}$ 1/h.

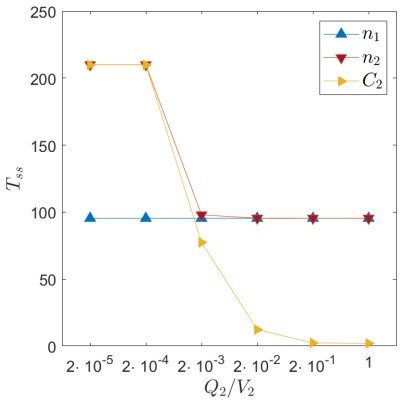

(b) Steady-state times for varying Q_2/V_2.

Figure 10: **Evolutionary timescale dependency on the vascularisation of the metastatic site.** Time evolution of the drug concentration and steady-state times obtained from numerical simulations of the model under the baseline scenario, for an intravenously-injected drug dose of 2.6915 μg/s, and final time $T = 210$ days, varying the blood flow-to-volume ratio in the metastatic site Q_2/V_2. In (a) we set $Q_2/V_2 = 2 \cdot 10^{-3}$ 1/h, leaving the other parameters at their reference value, and display the drug concentration in the central (blue), peripheral (orange), primary tumour (yellow) and metastatic tumour (purple) compartments, up to day 105. In (b) we display the steady-state times for n_1 (blue), n_2 (red) and C_2 (yellow) for different values of the ratio Q_2/V_2, specifically $Q_2/V_2 \in \{2 \cdot 10^{-5}, 2 \cdot 10^{-4}, 2 \cdot 10^{-3}, 2 \cdot 10^{-2}, 2 \cdot 10^{-1}, 1\}$ 1/h. The steady state time is the first time at which $D_{i,k} < tol$, with $D_{i,k}$ defined in (35) and a tolerance of $tol = 10^{-6}$. More details on the simulation set-up and numerical methods can be found in Section 4.1.

We performed global sensitivity analysis and long-term numerical simulations of the full system, to verify the analytical results outside the asymptotic regime of rare phenotypic changes due to epimutations, and to better understand the consequences of cancer adaptive dynamics on the outcome of treatment. To do so we adopted a case study of metastatic melanoma under Dabrafenib monotherapy, through which we could gain deeper insights into the impact of tissue-specific physiological parameters and drug kinetics on the evolution of the metastatic cancer. We found that the tumour stage and its location may influence *in situ* drug distribution during the course of treatment (Ziemys et al., 2018). In particular, the tumour angiogenic switch and the organ characteristics may affect the overall level of tumour vascularisation, regulating the timeline of local drug delivery. Moreover, the tissue drug affinity of the tumour, *i.e.* the tissue-to-plasma partition coefficient, regulates the maximum local concentration of cytotoxic compound. As a consequence, discrepancies in drug concentrations between the two tumour sites may arise during treatment, resulting in differing local environments to which cells will adapt. In line with the results of the asymptotic analysis, this fosters phenotypic diversity among tumours at different locations and the emergence of distinct subclones (Tsuruo and Fidler, 1981; Yancovitz et al., 2012).

In particular, assuming that the primary tumour has significantly increased its vascular supply prior to undergoing metastatic spread, the fast increase in the local concentration of the cytotoxic drug will speed up the selection of more resistant phenotypic traits in the primary tumour. Conversely, assuming the metastasis is yet to undergo substantial angiogenesis for further dispersal, the expected lower vascular supply of the secondary tumour should result in a slower increase in drug concentration at this site. Further assuming lower drug affinity of the metastatic tumour, this correlates with a lower selective pressure in the metastatic site which, together with the selection of cells with higher migratory abilities in the primary tumour, favours the emergence of a subpopulation of highly drug-resistant cells in the metastasis, in agreement with the results of the asymptotic analysis. Overall, this confers further evolutionary advantage to the tumour population, as it will have a higher chance of survival to sudden environmental changes, a big trade off feature of biological dispersal despite leaving the primary site may be a risk for tumour cells. This is coherent with empirical studies suggesting that chemotherapy fosters metastatisation and may provide an explanation for the evidence indicating that the metastatic site is often less impacted by chemotherapy (D'Alterio et al., 2020; Massagué and Obenauf, 2016; Obenauf et al., 2015; Parker et al., 2022).

Finally, investigating the impact of drug kinetics on cancer evolution under the twice-a-day oral adminis-

tration protocol used in the clinic, we observed that the pharmacokinetics and the cancer adaptive dynamics evolve on different timescales, *i.e.* hours vs. days. This discrepancy implies that the long-term evolutionary outcome of treatment may not be significantly influenced by short-term PK dynamics and fluctuations of the *in situ* drug concentration, but rather by average cytotoxic levels throughout the duration of chemotherapy, especially when the drug dose is particularly high. Then, considering a constant drug regimen reproducing analogous evolutionary outcomes, we observed that the time at which the phenotypic distributions in the two sites reach steadiness are larger than the median time of response and below the median treatment durations for the selected case study. This suggests that the time of response may correlate to the system being sufficiently close to steady state, and that such information may be relevant to avoid unnecessary prolongation of treatment.

5.2 Strengths of the model and methodology

A key strength of our approach lies in the adoption of structured models to represent the cancer cell populations in different sites, which allow us to effectively capture both intra- and inter-tumour phenotypic heterogeneity, particularly in relation to cell resistance to chemotherapy. The type of model proposed, *i.e.* one composed of PDEs of the non-local Fisher-KPP type, is grounded in a robust mathematical theory that facilitates analytical investigations, enabling us to get information on the long-term dynamics of the system in a wide range of parameter values and, therefore, biological scenarios. By considering distinct populations for the primary tumour and the metastases, each with its own site-specific environmental conditions, and incorporating the connectivity between these sites, we achieve a more detailed understanding of the evolution of chemoresistance in metastatic tumours, notoriously complex to treat. The integration of a PK model enables realistic drug delivery dynamics and physiological differences among tumour tissues, two key factors contributing to such complexity, to be captured. Moreover, the PK model can be calibrated with parameters estimated from *in vivo* or *ex vivo* data, readily available in the existing literature for the carefully selected case study.

Notably, the adopted methodology for numerical simulations enabled us to reproduce the evolutionary outcomes predicted under realistic "twice-a-day" delivery schedule using a constant drug regimen. While such regimen is not clinically applicable, at least for the selected case study, it enables a deeper analysis on the treatment advancement by exploiting the convergence of the solution of the system to some equilibrium. This strategy can be of great use for follow-up investigations such as, for instance, optimal control studies aimed at finding the most effective treatment strategy, thus enhancing the potential for real-life impact of the model. Ultimately, the scale of such impact will be widened by the flexibility of the modelling framework, which can be adapted to various types of tumours, a variable number of metastases, and diverse drug delivery protocols.

5.3 Limitations and perspectives

Cell migration and metastatic spread We chose the migration rate $\nu_{1,2}(y)$ to significantly increase only as the phenotypic state of a cell gets closer to the highest levels of drug resistance, but it would be relevant to consider alternative definitions, in particular non-smooth ones, as they might better reflect the switch in the intravasation ability of cancer cells as they become more aggressive. The use of different definitions for $\nu_{1,2}(y)$ in the PDE for n_1 and that for n_2 would also be relevant in view of the fact that successful intravasation of cancer cells does not necessarily correlate with survival in the circulation and successful extravasation to the metastatic site. In fact, circulating tumour cells in the bloodstream may be attacked by the immune system and face the challenge of adhesion to the vascular walls to exit the circulation, and may potentially endow themselves with more resistant traits (Fidler, 2003). The addition of a PDE describing the evolutionary dynamics of circulating tumour cells may therefore provide a more realistic extension of our modelling framework, which currently relies on the limiting assumption that cells exiting the primary tumour will immediately appear in the metastatic site maintaining their original phenotypic state. In addition, the extension of this model to one including motion between several patches, *e.g.* as proposed by Mirrahimi (2012), could be used to investigate more complex dynamics arising in cancers presenting multiple metastatic sites. This could allow for the theoretical exploration of the *seed and soil* hypothesis (Fidler, 2003) of metastatic spread, accounting for different extravasation probabilities to different sites, *e.g.* as done by Franssen et al. (2019). Moreover, this mathematical framework may help explain why

secondary seeding is much more efficient at spreading cells than dispersal from the primary site (Scott et al., 2013a; Vitos and Gerlee, 2022), thanks to promising results of previous studies on host-pathogen interactions (Alfaro et al., 2023; Hamel et al., 2021) analysing how pathogen persistence is mediated by the presence of a middle host.

Cell proliferation and tumour burden Building upon the strategies presented by Almeida et al. (2019); Villa et al. (2021), in our model we took into account a one-dimensional phenotypic trait whereby higher levels of drug resistance correlate with lower proliferation rates of cancer cells (Chu and Sartorelli, 2004; Corrie, 2011). Nevertheless, subclones simultaneously exhibiting high proliferation rates and high levels of drug resistance may exist (Sharma et al., 2010). It would therefore be biologically significant to consider a two-dimensional phenotypic state, as previously done by Chisholm et al. (2015), to capture the phenotypic evolution of tumours without any *a priori* assumption of a link between the level of drug tolerance and proliferation potential of the cells. This may affect the relation, emergent from the model, between the development of resistance and the evolution of the tumour burden during therapy. On this note, it is important to remark that we included the tumour volume V_i as a physiological parameter in the PK model, but kept this quantity constant throughout the simulations, for the sake of simplicity. Indeed the tumour volume is dependent on the number of cancer cells composing it, and it would therefore be significant to allow V_i to vary in time as a function of the cell number I_i in future work. This would allow to account for the impact on the drug delivery of changes in the tumour burden expected to occur during chemotherapy.

Therapeutic strategy and personalised treatment Given the novelty of this work, we here restricted our attention to a case study of BRAF-mutated melanoma under Dabrafenib monotherapy. In the clinic, however, this is usually combined with Trametinib (Long et al., 2017), a kinase inhibitor of MEK protein adopted to prevent the development of resistance to the BRAF inhibitor (Luebker and Koepsell, 2019). Therefore, future work investigating the development of drug resistance in metastatic melanoma under treatment should extend this modelling framework to include a PK model for Trametinib, as done by Sun et al. (2016), and its drug resistance-inhibiting effect on cancer cells, *e.g.* modelled via a drift in phenotypic space, being aware that compounds interact with each other when administered simultaneously. Moreover, while in this theoretical study we adopted parameter values collected from the literature, in order to employ this model for treatment optimisation purposes, it should rely on patient-specific data to improve reliability. To achieve this it is necessary to collect *ex vivo* data on plasma and tissue compound concentrations, and use them for model calibration using a two-stage approach, as done by Himstedt et al. (2020). First, one should estimate the systemic PK parameters, *i.e.* the ones related to central and peripheral compartments, based on the plasma concentration-time profile. Secondly, tissue concentration–time profiles should be used to estimate the remaining tissue-specific parameters. We note, however, that experimental methods to measure the partition coefficient parameters, independently of the mathematical model, do exist (Holt et al., 2019).

Credit authorship contribution statement

Federica Padovano: Conceptualization, Formal analysis, Investigation, Methodology, Software, Visualization, Writing - original draft. **Chiara Villa**: Conceptualization, Formal analysis, Funding acquisition, Methodology, Supervision, Writing - review & editing.

Declaration of competing interest

The authors declare that they have no known competing financial interests or personal relationships that could have appeared to influence the work reported in this paper.

Acknowledgements and Funding

Acknowledgments The authors thank Luis Almeida (LJLL, Sorbonne Université, FR), Tommaso Lorenzi (Politecnico di Torino, IT) and Marco Picasso (EPFL, CH) for the insightful discussions in the initial stages of the project.

Funding This project has received funding from the European Union's Horizon 2020 research and innovation programme under the Marie Skłodowska-Curie grant agreement No 945298-ParisRegionFP. C.V. is a Fellow of the Paris Region Fellowship Programme, supported by the Paris Region.

References

T. A. Ahmed. *Pharmacokinetics of drugs following IV bolus, IV infusion, and oral administration*, volume 10. IntechOpen Rijeka, 2015.

M. Alfaro, F. Hamel, F. Patout, and L. Roques. Adaptation in a heterogeneous environment II: To be three or not to be. *Journal of Mathematical Biology*, 87(5):68, 2023.

L. Almeida, P. Bagnerini, G. Fabrini, B. D. Hughes, and T. Lorenzi. Evolution of cancer cell populations under cytotoxic therapy and treatment optimisation: insight from a phenotype-structured model. *ESAIM: Mathematical Modelling and Numerical Analysis*, 53(4):1157–1190, 2019.

D. Balakirouchenane, S. Guégan, C. Csajka, A. Jouinot, V. Heidelberger, A. Puszkiel, O. Zehou, N. Khoudour, P. Courlet, N. Kramkimel, et al. Population pharmacokinetics/pharmacodynamics of dabrafenib plus trametinib in patients with BRAF-mutated metastatic melanoma. *Cancers*, 12(4):931, 2020.

G. Barles, L. C. Evans, and P. E. Souganidis. Wavefront propagation for reaction-diffusion systems of PDE. *Duke Mathematical Journal*, 61(3):835 – 858, 1990.

G. Barles, S. Mirrahimi, and B. Perthame. Concentration in Lotka-Volterra parabolic or integral equations: a general convergence result. *Methods and Applications of Analysis*, 16(3):321–340, 2009.

V. Boussange and L. Pellissier. Eco-evolutionary model on spatial graphs reveals how habitat structure affects phenotypic differentiation. *Communications Biology*, 5(1):668, 2022.

S. Bowyer, R. Lee, A. Fusi, and P. Lorigan. Dabrafenib and its use in the treatment of metastatic melanoma. *Melanoma Management*, 2(3):199–208, 2015.

G. W. Brodland and J. H. Veldhuis. The mechanics of metastasis: insights from a computational model. 2012.

J. Budczies, M. von Winterfeld, F. Klauschen, M. Bockmayr, J. K. Lennerz, C. Denkert, T. Wolf, A. Warth, M. Dietel, I. Anagnostopoulos, et al. The landscape of metastatic progression patterns across major human cancers. *Oncotarget*, 6(1):570, 2015.

K. Bukowski, M. Kciuk, and R. Kontek. Mechanisms of multidrug resistance in cancer chemotherapy. *International journal of molecular sciences*, 21(9):3233, 2020.

I. M. Bulai, M. C. De Bonis, C. Laurita, and V. Sagaria. Modeling metastatic tumor evolution, numerical resolution and growth prediction. *Mathematics and Computers in Simulation*, 203:721–740, 2023.

L. C. Cabaco, A. Tomas, M. Pojo, and D. C. Barral. The dark side of melanin secretion in cutaneous melanoma aggressiveness. *Frontiers in Oncology*, 12:887366, 2022.

F. Campolongo, A. Saltelli, and J. Cariboni. From screening to quantitative sensitivity analysis. a unified approach. *Computer physics communications*, 182(4):978–988, 2011.

R. H. Chisholm, T. Lorenzi, A. Lorz, A. K. Larsen, L. N. d. Almeida, A. Escargueil, and J. Clairambault. Emergence of drug tolerance in cancer cell populations: an evolutionary outcome of selection, nongenetic instability, and stress-induced adaptation. *Cancer research*, 75(6):930–939, 2015.

R. H. Chisholm, T. Lorenzi, and J. Clairambault. Cell population heterogeneity and evolution towards drug resistance in cancer: biological and mathematical assessment, theoretical treatment optimisation. *Biochimica et Biophysica Acta (BBA)-General Subjects*, 1860(11):2627–2645, 2016a.

R. H. Chisholm, T. Lorenzi, and A. Lorz. Effects of an advection term in nonlocal lotka–volterra equations. *Communications in mathematical sciences*, 14(4):1181–1188, 2016b.

H. Cho and D. Levy. Modeling the dynamics of heterogeneity of solid tumors in response to chemotherapy. *Bulletin of Mathematical Biology*, 79:2986–3012, 2017.

H. Cho and D. Levy. Modeling continuous levels of resistance to multidrug therapy in cancer. *Applied Mathematical Modelling*, 64:733–751, 2018a.

H. Cho and D. Levy. Modeling the chemotherapy-induced selection of drug-resistant traits during tumor growth. *Journal of theoretical biology*, 436:120–134, 2018b.

H. Cho and D. Levy. The impact of competition between cancer cells and healthy cells on optimal drug delivery. *Mathematical Modelling of Natural Phenomena*, 15:42, 2020.

E. Chu and A. Sartorelli. Cancer chemotherapy. *Basic & Clinical Pharmacology*, 2004.

J. Clairambault. An evolutionary perspective on cancer, with applications to anticancer drug resistance modelling and perspectives in therapeutic control. *Journal of Mathematical Study*, pages 1–21, 2019.

J. Clairambault and C. Pouchol. A survey of adaptive cell population dynamics models of emergence of drug resistance in cancer, and open questions about evolution and cancer. *Biomath*, 8(1):23, 2019.

P. G. Corrie. Cytotoxic chemotherapy: clinical aspects. *Medicine*, 39(12):717–722, 2011.

C. Cuenod and D. Balvay. Perfusion and vascular permeability: basic concepts and measurement in DCE-CT and DCE-MRI. *Diagnostic and interventional imaging*, 94(12):1187–1204, 2013.

I. Dagogo-Jack and A. T. Shaw. Tumour heterogeneity and resistance to cancer therapies. *Nature reviews Clinical oncology*, 15(2):81–94, 2018.

M. Delitala and T. Lorenzi. A mathematical model for progression and heterogeneity in colorectal cancer dynamics. *Theoretical population biology*, 79(4):130–138, 2011.

L. Desvillettes, P. E. Jabin, S. Mischler, and G. Raoul. On selection dynamics for continuous structured populations. *Communications in Mathematical Sciences*, 6(3):729–747, 2008.

D. Diego, G. F. Calvo, and V. M. Pérez-García. Modeling the connection between primary and metastatic tumors. *Journal of mathematical biology*, 67:657–692, 2013.

O. Diekmann, P.-E. Jabin, S. Mischler, and B. Perthame. The dynamics of adaptation: an illuminating example and a Hamilton–Jacobi approach. *Theoretical population biology*, 67(4):257–271, 2005.

W. Doerfler and P. Böhm. *DNA methylation: development, genetic disease and cancer*, volume 310. Springer Science & Business Media, 2006.

P. Duesberg, R. Stindl, and R. Hehlmann. Explaining the high mutation rates of cancer cells to drug and multidrug resistance by chromosome reassortments that are catalyzed by aneuploidy. *Proceedings of the National Academy of Sciences*, 97(26):14295–14300, 2000.

C. D'Alterio, S. Scala, G. Sozzi, L. Roz, and G. Bertolini. Paradoxical effects of chemotherapy on tumor relapse and metastasis promotion. In *Seminars in cancer biology*, volume 60, pages 351–361. Elsevier, 2020.

European Medicine Agency. EMA/CHMP/242419/2013/corr 1 - CHMP assessment report: Tafinlar. `https://www.ema.europa.eu/en/documents/product-information/tafinlar-epar-product-information_en.pdf`, 2013.

L. C. Evans. *Partial differential equations*, volume 19. American Mathematical Society, 2022.

I. J. Fidler. The pathogenesis of cancer metastasis: the 'seed and soil' hypothesis revisited. *Nature reviews cancer*, 3(6):453–458, 2003.

W. H. Fleming and P. E. Souganidis. PDE-viscosity solution approach to some problems of large deviations. *Annali della Scuola Normale Superiore di Pisa-Classe di Scienze*, 13(2):171–192, 1986.

L. C. Franssen, T. Lorenzi, A. E. Burgess, and M. A. Chaplain. A mathematical framework for modelling the metastatic spread of cancer. *Bulletin of mathematical biology*, 81:1965–2010, 2019.

J. M. Gallo, P. Vicini, A. Orlansky, S. Li, F. Zhou, J. Ma, S. Pulfer, M. A. Bookman, and P. Guo. Pharmacokinetic model-predicted anticancer drug concentrations in human tumors. *Clinical cancer research*, 10 (23):8048–8058, 2004.

A. Ghaffari, B. Bahmaie, and M. Nazari. A mixed radiotherapy and chemotherapy model for treatment of cancer with metastasis. *Mathematical methods in the applied sciences*, 39(15):4603–4617, 2016.

R. J. Gillies, D. Verduzco, and R. A. Gatenby. Evolutionary dynamics of carcinogenesis and why targeted therapy does not work. *Nature Reviews Cancer*, 12(7):487–493, 2012.

J. D. Gordan, J. A. Bertout, C.-J. Hu, J. A. Diehl, and M. C. Simon. HIF-2α promotes hypoxic cell proliferation by enhancing c-myc transcriptional activity. *Cancer cell*, 11(4):335–347, 2007.

M. M. Gottesman. Mechanisms of cancer drug resistance. *Annual review of medicine*, 53(1):615–627, 2002.

G. P. Gupta and J. Massagué. Cancer metastasis: building a framework. *Cell*, 127(4):679–695, 2006.

F. Hamel, F. Lavigne, and L. Roques. Adaptation in a heterogeneous environment I: persistence versus extinction. *Journal of Mathematical Biology*, 83:1–42, 2021.

N. Hartung, S. Mollard, D. Barbolosi, A. Benabdallah, G. Chapuisat, G. Henry, S. Giacometti, A. Iliadis, J. Ciccolini, C. Faivre, et al. Mathematical modeling of tumor growth and metastatic spreading: validation in tumor-bearing mice. *Cancer research*, 74(22):6397–6407, 2014.

A. Himstedt, C. Braun, S. G. Wicha, and J. M. Borghardt. Towards a quantitative mechanistic understanding of localized pulmonary tissue retention—A combined in vivo/in silico approach based on four model drugs. *Pharmaceutics*, 12(5):408, 2020.

K. Holt, M. Ye, S. Nagar, and K. Korzekwa. Prediction of tissue-plasma partition coefficients using microsomal partitioning: Incorporation into physiologically based pharmacokinetic models and steady-state volume of distribution predictions. *Drug metabolism and disposition*, 47(10):1050–1060, 2019.

P.-E. Jabin and R. S. Schram. Selection-Mutation dynamics with spatial dependence. *Journal de Mathématiques Pures et Appliquées*, 176, 2016.

H. Jones and K. Rowland-Yeo. Basic concepts in physiologically based pharmacokinetic modeling in drug discovery and development. *CPT: pharmacometrics & systems pharmacology*, 2(8):1–12, 2013.

G. S. Karagiannis, J. S. Condeelis, and M. H. Oktay. Chemotherapy-induced metastasis: mechanisms and translational opportunities. *Clinical & experimental metastasis*, 35:269–284, 2018.

A. Kiparissides, S. Kucherenko, A. Mantalaris, and E. Pistikopoulos. Global sensitivity analysis challenges in biological systems modeling. *Industrial & Engineering Chemistry Research*, 48(15):7168–7180, 2009.

A. W. Lambert, D. R. Pattabiraman, and R. A. Weinberg. Emerging biological principles of metastasis. *Cell*, 168(4):670–691, 2017.

O. Lavi, J. M. Greene, D. Levy, and M. M. Gottesman. The role of cell density and intratumoral heterogeneity in multidrug resistance. *Cancer research*, 73(24):7168–7175, 2013.

O. Lavi, J. M. Greene, D. Levy, and M. M. Gottesman. Simplifying the complexity of resistance heterogeneity in metastasis. *Trends in molecular medicine*, 20(3):129–136, 2014.

C. K. Li. The glucose distribution in 9L rat brain multicell tumor spheroids and its effect on cell necrosis. *cancer*, 50(10):2066–2073, 1982.

S. Lion, M. Boots, and A. Sasaki. Multimorph eco-evolutionary dynamics in structured populations. *The American Naturalist*, 200(3):345–372, 2022.

G. Long, K. Flaherty, D. Stroyakovskiy, H. Gogas, E. Levchenko, F. De Braud, J. Larkin, C. Garbe, T. Jouary, A. Hauschild, et al. Dabrafenib plus trametinib versus dabrafenib monotherapy in patients with metastatic BRAF V600E/K-mutant melanoma: long-term survival and safety analysis of a phase 3 study. *Annals of Oncology*, 28(7):1631–1639, 2017.

T. Lorenzi, R. H. Chisholm, and J. Clairambault. Tracking the evolution of cancer cell populations through the mathematical lens of phenotype-structured equations. *Biology direct*, 11:1–17, 2016.

T. Lorenzi, C. Venkataraman, A. Lorz, and M. A. Chaplain. The role of spatial variations of abiotic factors in mediating intratumour phenotypic heterogeneity. *Journal of theoretical biology*, 451:101–110, 2018.

A. Lorz, S. Mirrahimi, and B. Perthame. Dirac mass dynamics in multidimensional nonlocal parabolic equations. *Communications in Partial Differential Equations*, 36(6):1071–1098, 2011.

S. A. Luebker and S. A. Koepsell. Diverse mechanisms of BRAF inhibitor resistance in melanoma identified in clinical and preclinical studies. *Frontiers in oncology*, 9:268, 2019.

S. Martin-Algarra, R. Hinshelwood, S. Mesnage, J. Cebon, P. F. Ferrucci, M. Aglietta, B. Neyns, V. Chiarion-Sileni, C. R. Lindsay, M. Del Vecchio, et al. Effectiveness of dabrafenib in the treatment of patients with BRAF V600–mutated metastatic melanoma in a Named Patient Program. *Melanoma research*, 29(5): 527–532, 2019.

J. Massagué and A. C. Obenauf. Metastatic colonization by circulating tumour cells. *Nature*, 529(7586): 298–306, 2016.

F. Michor and Y. Iwasa. Dynamics of metastasis suppressor gene inactivation. *Journal of theoretical biology*, 241(3):676–689, 2006.

F. Michor, M. A. Nowak, and Y. Iwasa. Stochastic dynamics of metastasis formation. *Journal of Theoretical Biology*, 240(4):521–530, 2006.

S. Mirrahimi. Adaptation and migration of a population between patches. *Discrete and Continuous Dynamical Systems-B*, 18(3):753–768, 2012.

S. Mirrahimi and S. Gandon. Evolution of specialization in heterogeneous environments: equilibrium between selection, mutation and migration. *Genetics*, 214(2):479–491, 2020.

S. Mirrahimi and B. Perthame. Asymptotic analysis of a selection model with space. *Journal de Mathématiques Pures et Appliquées*, 104(6):1108–1118, 2015.

R. K. Mittapalli, S. Vaidhyanathan, A. Z. Dudek, and W. F. Elmquist. Mechanisms limiting distribution of the threonine-protein kinase B-RaFV600E inhibitor dabrafenib to the brain: implications for the treatment of melanoma brain metastases. *Journal of Pharmacology and Experimental Therapeutics*, 344(3):655–664, 2013.

D. M. Moss and M. Siccardi. Optimizing nanomedicine pharmacokinetics using physiologically based pharmacokinetics modelling. *British journal of pharmacology*, 171(17):3963–3979, 2014.

P. K. Newton, J. Mason, K. Bethel, L. Bazhenova, J. Nieva, L. Norton, and P. Kuhn. Spreaders and sponges define metastasis in lung cancer: a markov chain monte carlo mathematical model. *Cancer research*, 73 (9):2760–2769, 2013.

P. K. Newton, J. Mason, N. Venkatappa, M. S. Jochelson, B. Hurt, J. Nieva, E. Comen, L. Norton, and P. Kuhn. Spatiotemporal progression of metastatic breast cancer: a markov chain model highlighting the role of early metastatic sites. *NPJ breast cancer*, 1(1):1–9, 2015.

D. X. Nguyen and J. Massagué. Genetic determinants of cancer metastasis. *Nature Reviews Genetics*, 8(5): 341–352, 2007.

E. Norris, J. R. King, and H. M. Byrne. Modelling the response of spatially structured tumours to chemotherapy: Drug kinetics. *Mathematical and Computer Modelling*, 43(7-8):820–837, 2006.

A. C. Obenauf, Y. Zou, A. L. Ji, S. Vanharanta, W. Shu, H. Shi, X. Kong, M. C. Bosenberg, T. Wiesner, N. Rosen, et al. Therapy-induced tumour secretomes promote resistance and tumour progression. *Nature*, 520(7547):368–372, 2015.

B. Ocaña-Tienda and V. M. Pérez-García. Mathematical modeling of brain metastases growth and response to therapies: A review. *Mathematical Biosciences*, page 109207, 2024.

A. Olivier and C. Pouchol. Combination of direct methods and homotopy in numerical optimal control: application to the optimization of chemotherapy in cancer. *Journal of Optimization Theory and Applications*, 181:479–503, 2019.

K. Pantel and M. Speicher. The biology of circulating tumor cells. *Oncogene*, 35(10):1216–1224, 2016.

A. L. Parker, M. Benguigui, J. Fornetti, E. Goddard, S. Lucotti, J. Insua-Rodríguez, A. P. Wiegmans, and E. C. L. C. of the Metastasis Research Society. Current challenges in metastasis research and future innovation for clinical translation. *Clinical & Experimental Metastasis*, 39(2):263–277, 2022.

B. Perthame. *Transport equations in biology*. Springer Science & Business Media, 2006.

B. Perthame and G. Barles. Dirac concentrations in lotka-volterra parabolic pdes. *Indiana University Mathematics Journal*, pages 3275–3301, 2008.

C. Pouchol, J. Clairambault, A. Lorz, and E. Trélat. Asymptotic analysis and optimal control of an integro-differential system modelling healthy and cancer cells exposed to chemotherapy. *Journal de Mathématiques Pures et Appliquées*, 116:268–308, 2018.

A. Puszkiel, G. Noé, A. Bellesoeur, N. Kramkimel, M.-N. Paludetto, A. Thomas-Schoemann, M. Vidal, F. Goldwasser, E. Chatelut, and B. Blanchet. Clinical pharmacokinetics and pharmacodynamics of dabrafenib. *Clinical Pharmacokinetics*, 58:451–467, 2019.

G. Qian and A. Mahdi. Sensitivity analysis methods in the biomedical sciences. *Mathematical biosciences*, 323:108306, 2020.

I. Ramis-Conde, M. A. Chaplain, A. R. Anderson, and D. Drasdo. Multi-scale modelling of cancer cell intravasation: the role of cadherins in metastasis. *Physical biology*, 6(1):016008, 2009.

A. Saltelli. Making best use of model evaluations to compute sensitivity indices. *Computer physics communications*, 145(2):280–297, 2002.

P. Schlicke, C. Kuttler, and C. Schumann. How mathematical modeling could contribute to the quantification of metastatic tumor burden under therapy: insights in immunotherapeutic treatment of non-small cell lung cancer. *Theoretical Biology and Medical Modelling*, 18(1):11, 2021.

J. G. Scott, D. Basanta, A. R. Anderson, and P. Gerlee. A mathematical model of tumour self-seeding reveals secondary metastatic deposits as drivers of primary tumour growth. *Journal of The Royal Society Interface*, 10(82):20130011, 2013a.

J. G. Scott, P. Gerlee, D. Basanta, A. G. Fletcher, P. K. Maini, and A. R. Anderson. Mathematical modeling of the metastatic process. *Experimental Metastasis: Modeling and Analysis*, pages 189–208, 2013b.

R. Sharma and S. Sharma. *Physiology, Blood Volume*. StatPearls, StatPearls Publishing, 2022.

S. V. Sharma, D. Y. Lee, B. Li, M. P. Quinlan, F. Takahashi, S. Maheswaran, U. McDermott, N. Azizian, L. Zou, M. A. Fischbach, et al. A chromatin-mediated reversible drug-tolerant state in cancer cell subpopulations. *Cell*, 141(1):69–80, 2010.

T. Shibue and R. A. Weinberg. EMT, CSCs, and drug resistance: the mechanistic link and clinical implications. *Nature reviews Clinical oncology*, 14(10):611–629, 2017.

X. Sun, J. Bao, and Y. Shao. Mathematical modeling of therapy-induced cancer drug resistance: connecting cancer mechanisms to population survival rates. *Scientific reports*, 6(1):22498, 2016.

S. Sundararajan, A. M. Thida, S. Yadlapati, and S. Koya. *Metastatic Melanoma*. StatPearls, 2022.

T. Tsuruo and I. J. Fidler. Differences in drug sensitivity among tumor cells from parental tumors, selected variants, and spontaneous metastases. *Cancer Research*, 41(8):3058–3064, 1981.

N. C. Turner and J. S. Reis-Filho. Genetic heterogeneity and cancer drug resistance. *The lancet oncology*, 13(4):e178–e185, 2012.

US Food and Drug Administration. Dabrafenib (Tafinlar) Pharmacology Review. `https://www.accessdata.fda.gov/drugsatfda_docs/label/2022/202806s022lbl.pdf`, 2013.

C. Villa, M. A. Chaplain, and T. Lorenzi. Evolutionary dynamics in vascularised tumours under chemotherapy: Mathematical modelling, asymptotic analysis and numerical simulations. *Vietnam Journal of Mathematics*, 49:143–167, 2021.

N. Vitos and P. Gerlee. Model-based inference of metastatic seeding rates in de novo metastatic breast cancer reveals the impact of secondary seeding and molecular subtype. *Scientific Reports*, 12(1):9455, 2022.

X. Wang, H. Zhang, and X. Chen. Drug resistance and combating drug resistance in cancer. *Cancer drug resistance*, 2(2):141, 2019.

J. P. Ward and J. R. King. Mathematical modelling of avascular-tumour growth. *Mathematical Medicine and Biology: A Journal of the IMA*, 14(1):39–69, 1997.

World Health Organization. Global Cancer Observatory. `https://gco.iarc.fr/`, 2022.

A. Wu, K. Loutherback, G. Lambert, L. Estévez-Salmerón, T. D. Tlsty, R. H. Austin, and J. C. Sturm. Cell motility and drug gradients in the emergence of resistance to chemotherapy. *Proceedings of the National Academy of Sciences*, 110(40):16103–16108, 2013.

M. Yancovitz, A. Litterman, J. Yoon, E. Ng, R. L. Shapiro, R. S. Berman, A. C. Pavlick, F. Darvishian, P. Christos, M. Mazumdar, et al. Intra-and inter-tumor heterogeneity of BRAFV600E mutations in primary and metastatic melanoma. *PloS one*, 7(1):e29336, 2012.

A. Yin, D. J. A. Moes, J. G. van Hasselt, J. J. Swen, and H.-J. Guchelaar. A review of mathematical models for tumor dynamics and treatment resistance evolution of solid tumors. *CPT: pharmacometrics & systems pharmacology*, 8(10):720–737, 2019.

Q. Zhou, P. Guo, G. D. Kruh, P. Vicini, X. Wang, and J. M. Gallo. Predicting human tumor drug concentrations from a preclinical pharmacokinetic model of temozolomide brain disposition. *Clinical Cancer Research*, 13(14):4271–4279, 2007.

A. Ziemys, K. Yokoi, M. Kai, Y. Liu, M. Kojic, V. Simic, M. Milosevic, A. Holder, and M. Ferrari. Progression-dependent transport heterogeneity of breast cancer liver metastases as a factor in therapeutic resistance. *Journal of controlled release*, 291:99–105, 2018.

H. Zou, P. Banerjee, S. S. Y. Leung, and X. Yan. Application of pharmacokinetic-pharmacodynamic modeling in drug delivery: development and challenges. *Frontiers in pharmacology*, 11:543082, 2020.

A Proofs of analytical results

A.1 Proof of the bounds on $I_{i\varepsilon}$

We prove the result by contradiction. Suppose that $0 < I_M < I_{1\varepsilon}$. We integrate $(24)_1$ and adopt the boundary conditions $(24)_3$ to obtain

$$\int_0^1 R_1(y, I_{1\varepsilon}) n_{1\varepsilon}(y) dy + \int_0^1 \nu_{2,1}(y) n_{1\varepsilon}(y) dy - \int_0^1 \nu_{1,2}(y) n_{1\varepsilon}(y) dy = 0\,. \tag{1}$$

For the first term of equation (1) we employ assumptions (15) and (22), along with the inequality $I_M < I_{1\varepsilon}$, to deduce

$$R_1(y, I_{1\varepsilon}) < R_1(y, I_M) \leq \max_{y\in[0,1]} \big(R_1(y, I_M)\big) \leq -\delta\,.$$

Multiplying both sides of this inequality by $n_{1\varepsilon}(y)$ and integrating, we obtain

$$\int_0^1 R_1(y, I_{1\varepsilon}) n_{1\varepsilon}(y) dy < \int_0^1 -\delta n_{1\varepsilon}(y) dy = -\delta I_{1\varepsilon}\,.$$

For what concerns the second and third terms of equation (1), from assumption (17) we can deduce

$$\int_0^1 \nu_{2,1}(y) n_{2\varepsilon}(y) dy \leq \nu_M I_{2\varepsilon} \quad \text{and} \quad -\int_0^1 \nu_{1,2}(y) n_{1\varepsilon}(y) dy \leq -\nu_m I_{1\varepsilon}\,.$$

Combining these results we obtain

$$0 = \int_0^1 R_1(y, I_{1\varepsilon}) n_{1\varepsilon}(y) dy + \int_0^1 \nu_{2,1}(y) n_{1\varepsilon}(y) dy - \int_0^1 \nu_{1,2}(y) n_{1\varepsilon}(y) dy < -\delta I_{1\varepsilon} + \nu_M I_{2\varepsilon} - \nu_m I_{1\varepsilon}\,,$$

and thus

$$I_{2\varepsilon} > \frac{(\nu_m + \delta)}{\nu_M} I_{1\varepsilon} > \frac{\nu_m}{\nu_M} I_{1\varepsilon} > \frac{\nu_m}{\nu_M} I_M\,. \tag{2}$$

Now we integrate equation $(24)_1$, both for $i = 1$ and $i = 2$, apply boundary conditions $(24)_3$, and then sum them to obtain

$$\int_0^1 R_1(y, I_{1\varepsilon}) n_{1\varepsilon}(y) dy + \int_0^1 R_2(y, I_{2\varepsilon}) n_{2\varepsilon}(y) dy = 0. \tag{3}$$

From assumption (15), inequality (2) and the technical assumption (22), we have that

$$R_1(y, I_{1\varepsilon}) < \max_{y\in[0,1]} \Big(R_1(y, I_M)\Big) \leq -\delta \quad \text{and} \quad R_2(y, I_{2\varepsilon}) < \max_{y\in[0,1]} \Big(R_2\big(y, \frac{\nu_m}{\nu_M} I_M\big)\Big) \leq -\delta\,.$$

Together with equation (3) and, again, the previous result (2), this gives

$$0 = \int_0^1 R_1(y, I_{1\varepsilon}) n_{1\varepsilon}(y) dy + \int_0^1 R_2(y, I_{2\varepsilon}) n_{2\varepsilon}(y) dy < -\delta(I_{1\varepsilon} + I_{2\varepsilon}) < -\delta\big(I_M + \frac{\nu_m}{\nu_M} I_M\big) < 0\,,$$

a contradiction. We thus conclude that $I_{1\varepsilon} \leq I_M$. The proof for the case with $0 < I_M < I_{2\varepsilon}$, and for the lower bounds of $I_{i\varepsilon}$ $(i = 1, 2)$ follow analogous arguments, relying on assumption (21).

A.2 Proof of the results for the asymptotic regime $\varepsilon \to 0$

We formally extend the analysis carried out by Mirrahimi (2012) for the case of constant migration rates to the case of phenotype-dependent migration rates.

Hopf-Cole transformation Following the work of Mirrahimi (2012), we introduce the Hopf-Cole transformation $n_{i\varepsilon}(y) = \exp\left(\frac{u_{i\varepsilon}(y)}{\varepsilon}\right)$ (Barles et al., 1990; Evans, 2022; Fleming and Souganidis, 1986), with $u_{i\varepsilon}(y)$ semi-convex (*i.e.* $\partial^2_{yy} u_{i\varepsilon} \geq -E$, for some constant $E > 0$), for $i = 1, 2$. Then we can evaluate

$$\frac{d^2 n_{i\varepsilon}}{dy^2} = \left(\varepsilon^{-1}\frac{d^2 u_{i\varepsilon}}{dy^2} + \varepsilon^{-2}\Big(\frac{du_{i\varepsilon}}{dy}\Big)^2\right) n_{i\varepsilon}\,,$$

and equation $(24)_1$ becomes

$$R_i\big(y, I_{i\varepsilon}\big)\, n_{i\varepsilon} + \varepsilon^2\left(\varepsilon^{-1}\frac{d^2 u_{i\varepsilon}}{dy^2} + \varepsilon^{-2}\Big(\frac{du_{i\varepsilon}}{dy}\Big)^2\right) n_{i\varepsilon} + \nu_{j,i}(y)\, n_{j\varepsilon} - \nu_{i,j}(y)\, n_{i\varepsilon} = 0, \qquad y \in (0,1).$$

We can rewrite the system $(24)_1$ for $n_{i\varepsilon}$ $(i = 1, 2)$ as the following steady-state system for $u_{i\varepsilon}$ $(i = 1, 2)$ in matrix-vector form:

$$\mathcal{A}_\varepsilon\, \mathcal{N}_\varepsilon = \mathcal{L}_\varepsilon\, \mathcal{N}_\varepsilon \tag{4}$$

where

$$\mathcal{A}_\varepsilon = \begin{pmatrix} R_1\big(y, I_{1\varepsilon}\big) - \nu_{1,2}(y) & \nu_{2,1}(y) \\ \nu_{1,2}(y) & R_2\big(y, I_{2\varepsilon}\big) - \nu_{2,1}(y) \end{pmatrix}, \tag{5}$$

$$\mathcal{N}_\varepsilon = \begin{pmatrix} n_{1\varepsilon} \\ n_{2\varepsilon} \end{pmatrix} = \begin{pmatrix} \exp\left(u_{1\varepsilon}/\varepsilon\right) \\ \exp\left(u_{2\varepsilon}/\varepsilon\right) \end{pmatrix}, \tag{6}$$

$$\mathcal{L}_\varepsilon = \operatorname{diag}\Big(-\varepsilon\frac{d^2 u_{1\varepsilon}}{dy^2} - \Big(\frac{du_{1\varepsilon}}{dy}\Big)^2, -\varepsilon\frac{d^2 u_{2\varepsilon}}{dy^2} - \Big(\frac{du_{2\varepsilon}}{dy}\Big)^2\Big). \tag{7}$$

Then given the eigenvalue $H_\varepsilon = H_\varepsilon(y, I_{1\varepsilon}, I_{2\varepsilon})$ of $\mathcal{A}_\varepsilon$ with corresponding eigenvector $\mathcal{N}_\varepsilon$, from (4) we have

$$\mathcal{L}_\varepsilon\, \mathcal{N}_\varepsilon = H_\varepsilon\, \mathcal{N}_\varepsilon\,, \tag{8}$$

which corresponds to the following equations for $u_{i\varepsilon}$

$$-\varepsilon\frac{d^2 u_{i\varepsilon}}{dy^2} - \Big(\frac{du_{i\varepsilon}}{dy}\Big)^2 = H_\varepsilon(y, I_{1\varepsilon}, I_{2\varepsilon}) \qquad i = 1, 2\,. \tag{9}$$

Hamilton-Jacobi equation Firstly, given the assumptions introduced in Section 3.1, from (25) and (26) we deduce that $n_{1\varepsilon}$ and $n_{2\varepsilon}$ converge weakly to measures n_1 and n_2, *i.e.*

$$n_{i\varepsilon}(y) \xrightarrow[\varepsilon\to 0]{*} n_i(y) \qquad i = 1, 2\,. \tag{10}$$

On the basis of the analysis carried out by Mirrahimi (2012) for the case of constant migration rates, we expect that in the asymptotic regime $\varepsilon \to 0$ both sequences $u_{1\varepsilon}$ and $u_{2\varepsilon}$ converge uniformly in $[0, 1]$ to a continuous function $u \in C([0, 1])$ and $(I_{1\varepsilon}, I_{2\varepsilon})$ converges to (I_1, I_2). We further assume that the semi-convexity of $u_{i\varepsilon}$ $(i = 1, 2)$ is preserved in the limit such that $u = u(y)$ is also semi-convex. If that is the case, then in the limit $\varepsilon \to 0$ equation (4) yields

$$\mathcal{A}\mathcal{N} = \mathcal{L}\mathcal{N} \tag{11}$$

where

$$\mathcal{A} = \begin{pmatrix} R_1\big(y, I_1\big) - \nu_{1,2}(y) & \nu_{2,1}(y) \\ \nu_{1,2}(y) & R_2\big(y, I_2\big) - \nu_{2,1}(y) \end{pmatrix}, \tag{12}$$

$$\mathcal{N} = \begin{pmatrix} n_1 \\ n_2 \end{pmatrix}, \tag{13}$$

$$\mathcal{L} = \operatorname{diag}\Big(-\Big(\frac{du}{dy}\Big)^2, -\Big(\frac{du}{dy}\Big)^2\Big). \tag{14}$$

Then as $\varepsilon \to 0$ equation (9) and the bounds (26) lead to the following constrained Hamilton-Jacobi equation for $u(y)$:

$$\begin{cases} -\Big(\dfrac{du}{dy}\Big)^2 = H(y, I_1, I_2) \\ \max\limits_{y\in[0,1]} u(y) = 0 \end{cases}, \tag{15}$$

where the constraint is required to ensure bounds on I_i $(i = 1, 2)$ in (26) are satisfied. Note that the right-hand-side of $(15)_1$ is zero at points $y_k \in \arg\max u(y)$ and negative for all $y \in [0, 1]$ that are not stationary points of $u(y)$. This implies

$$\begin{cases} H(y_k, I_1, I_2) = 0 & \forall\ y_k \in \arg\max u(y), \\ \max\limits_{y\in[0,1]} H(y, I_1, I_2) = 0, \end{cases} \tag{16}$$

where $H = H(y, I_1, I_2)$ is the largest eigenvalue of $\mathcal{A}$ with corresponding eigenvector $\mathcal{N}$. Hence H is given by

$$H(y, I_1, I_2) = F + \sqrt{F^2 - 4G}\,, \tag{17}$$

with

$$F = R_1(y, I_1) - \nu_{1,2}(y) + R_2(y, I_2) - \nu_{2,1}(y)\,, \tag{18}$$

$$G = \big(R_1(y, I_1) - \nu_{1,2}(y)\big)\big(R_2(y, I_2) - \nu_{2,1}(y)\big) - \nu_{1,2}(y)\nu_{2,1}(y)\,. \tag{19}$$

Note from (17) that for $(16)_1$ to be satisfied we must have that F is negative at each $y_k \in \arg\max u(y)$. In such case, (16) implies

$$\begin{cases} G(y_k, I_1, I_2) = 0 & \forall\ y_k \in \arg\max u(y) \\ \min\limits_{y\in[0,1]} G(y, I_1, I_2) = 0\,. \end{cases} \tag{20}$$

Then from (15) and (16) we have

$$\mathrm{supp}\big(n_i\big) \subset \Gamma \qquad i = 1, 2\,, \tag{21}$$

where

$$\Gamma := \arg\max_{y\in[0,1]} H(y) \equiv \big\{y \in [0, 1] : H(y, I_1, I_2) = 0\big\}\,, \tag{22}$$

which – under assumption (19) – we expect to be discrete and finite, with cardinality $K \in \mathbb{N}$.

Remark 1: *As we have shown that* (16)*, together with definitions* (17) *and* (18)*, implies* (20)*, we could alternatively define* Γ *in* (21) *as*

$$\Gamma := \arg\min_{y\in[0,1]} G(y) \equiv \big\{y \in [0, 1] : G(y, I_1, I_2) = 0\big\}\,.$$

Remark 2: *The support of* n_i *is only a proper subset of* Γ *as defined in* (22)*, since* Γ *includes both the points at which* u *attains its maxima and minima (from* $(15)_1$*), while* n_i *will be zero at the points in* $\arg\min u$ *(from* $(15)_2$*). Hence* (21) *may be more precisely written as*

$$\mathrm{supp}\big(n_i\big) \subseteq \Omega \subset \Gamma \qquad i = 1, 2\,,$$

where Γ *is defined as in* (22) *(or as in Remark 1) and* Ω *is defined as*

$$\Omega := \arg\max_{y\in[0,1]} u(y) \equiv \big\{y \in [0, 1] : u(y) = 0\big\}\,.$$

Concentration as Dirac masses. From (25), we deduce that, along subsequences and for $i = 1, 2$, $n_{i\varepsilon}$ converges weakly in the asymptotic regime $\varepsilon \to 0$ to a measure n_i. In view of the results so far obtained on the support of n_i, we have that the measures n_1 and n_2 to which $n_{1\varepsilon}$ and $n_{2\varepsilon}$ converge concentrate as Dirac masses, *i.e.*

$$n_{i\varepsilon}(y) \xrightarrow[\varepsilon\to 0]{*} \sum_{k=1}^{K} \rho_{ik}\, \delta(y - y_k) \qquad i = 1, 2\,, \tag{23}$$

where the points $y_k \in [0, 1]$ can be found by solving (16) – or alternatively (20) – while the weights $\rho_{ik} \geq 0$ must be such that

$$I_i = \sum_{k=1}^{K} \rho_{ik} \qquad i = 1, 2\,, \tag{24}$$

and can be found by integrating the system (11) over a ball $B_r(y_k) := \{y \in [0,1] : |y - y_k| \leq r\}$ centred at y_k, with radius r small enough that no other point in the support of n_i $(i = 1, 2)$ is contained in $B_r(y_k)$. This yields

$$\begin{cases} \big(R_1(y_k, I_1) - \nu_{1,2}(y_k)\big)\rho_{1k} + \nu_{2,1}(y_k)\rho_{2k} = 0 \\ \big(R_2(y_k, I_2) - \nu_{2,1}(y_k)\big)\rho_{2k} + \nu_{1,2}(y_k)\rho_{1k} = 0. \end{cases} \qquad k = 1, .., K \tag{25}$$

A.3 Proof the analytical results for the metastatic spread case

If $\nu_{1,2}(y) \geq 0$, with $\nu_{1,2}(y) > 0$ for some $y \in [0,1]$, and $\nu_{2,1}(y) \equiv 0$ for all $y \in [0,1]$, then solving (16) leads to the following systems:

$$\begin{cases} R_1(y_1, I_1) - \nu_{1,2}(y_1) = 0 \\ \partial_y R_1(y_1, I_1) - \partial_y \nu_{1,2}(y_1) = 0 \end{cases} \quad \text{and} \quad \begin{cases} R_2(y_2, I_2) = 0 \\ \partial_y R_2(y_2, I_2) = 0\,. \end{cases} \tag{26}$$

Notice that (26) together with assumption (20) ensure that F defined in (18) is negative at y_1 and y_2, as required by (16) and (17). From the second equation of each system in (26) we obtain y_1 and y_2, while from the first one of each system we get I_1 and I_2. Moreover, equations (24) and (25) result in

$$\rho_{11} = I_1\,, \quad \rho_{12} = 0 \quad \rho_{21} = \min\left(- \frac{\nu_{1,2}(y_1)}{R_2(y_1, I_2)}\rho_{11}, I_2 \right), \quad \rho_{22} = I_2 - \rho_{21}\,. \tag{27}$$

Solving (26) for $R_i(y, I_i)$ $(i = 1, 2)$ given by (7) and for $\nu_{1,2}(y)$ given by (9), we have that (10) and (23) corresponds to the following asymptotic solution:

$$n_1(y) = I_1\,\delta(y - y_1) \qquad \text{and} \qquad n_2(y) = \rho_{21}\,\delta(y - y_1) + \rho_{22}\,\delta(y - y_2)\,, \tag{28}$$

with

$$y_1 = \frac{b_1}{b_1 + \hat{\nu}_{1,2}} h_1\,, \qquad y_2 = h_2\,, \tag{29}$$

and

$$I_1 = \frac{1}{d_1}\left[a_1 - \frac{\hat{\nu}_{1,2} b_1 h_1^2}{b_1 + \hat{\nu}_{1,2}}\right], \quad I_2 = \frac{a_2}{d_2}\,, \qquad \rho_{21} = \min\left(\frac{\hat{\nu}_{1,2}\, y_1^2}{b_2(y_1 - h_2)^2} I_1, I_2\right), \quad \rho_{22} = I_2 - \rho_{21}\,. \tag{30}$$

The development of drug resistance in metastatic tumours under chemotherapy: an evolutionary perspective
Supplementary Material

Federica Padovano * Chiara Villa†

In this document (supplementary material) we report supplementary material to the contents of the above named publication (main publication). For details of the equations referred to in this document, please see the main publication.

1 Supplementary analytical results

The following analytical results extend those in Section 3.3 of the Main Manuscript to the case of localised tumour and secondary seeding. Therefore we refer to equations appearing in Section 3.3 and Appendix A.2 of the Main Manuscript.

1.1 Analytical results for the localised tumors case: $\nu_{1,2} \equiv 0$ and $\nu_{2,1} \equiv 0$

If both $\nu_{1,2}(y) \equiv 0$ and $\nu_{2,1}(y) \equiv 0$ for all $y \in [0,1]$, then solving (A.16) leads to the following systems:

$$\begin{cases} R_i(y_i, I_i) = 0 \\ \partial_y R_i(y_i, I_i) = 0 \end{cases} \qquad i = 1, 2\,. \tag{1}$$

Notice that (1) together with assumption (20) ensure that F defined in (A.18) is negative at y_1 and y_2, as required by (A.16) and (A.17). From $(1)_2$ we obtain y_1 and y_2, and from $(1)_1$ we get I_1 and I_2, while (A.25) leads to having $\rho_{21} = \rho_{12} = 0$ which together with (A.24) imply $\rho_{11} = I_1$ and $\rho_{22} = I_2$. Doing this for $R_i(y, I_i)$ $(i = 1, 2)$ given by (7) leads to the following solution:

$$n_i(y) = I_i\, \delta(y - y_i) \qquad \text{with} \qquad y_i = h_i\,, \quad I_i = \frac{a_i}{d_i} \qquad \text{for} \qquad i = 1, 2\,. \tag{2}$$

These results, in agreement with previous results in the literature focusing on a single localised tumour, provide a formal description of the fact that populations living in separate, non-communicating sites evolve independently of each other. Each population presents monomorphism at equilibrium, and the trait selected corresponds to the fittest trait h_i $(i = 1, 2)$ determined by the local environment. That is, of course, if cells were present in both sites initially: if the secondary site is representing a metastatic site, in this scenario no cells ever reach it and we expect $n_2 \equiv 0$ at equilibrium.

1.2 Analytical results for the secondary seeding case: $\nu_{1,2} \not\equiv 0$ and $\nu_{2,1} \not\equiv 0$

Consider now the case in which $\nu_{1,2} \not\equiv 0$ and $\nu_{2,1} \not\equiv 0$. In particular we focus on the case in which the selected traits y_k are such that $\nu_{i,j}(y_k) > 0$ $(i, j = 1, 2 \;\; i \neq j)$. In this case, for each $k = 1, .., K$ we have from $(A.25)_1$ that $\rho_{2k} > 0$ implies $\rho_{1k} > 0$ and $R_1(y_k, I_1) - \nu_{1,2}(y_k) < 0$. Similarly, from $(A.25)_2$ we have that $\rho_{1k} > 0$ implies $\rho_{2k} > 0$ and $R_2(y_k, I_2) - \nu_{2,1}(y_k) < 0$. Therefore we either have both $\rho_{1k} = \rho_{2k} = 0$ (trivial case) or $\rho_{1k} > 0$, $\rho_{2k} > 0$ and

$$R_i(y_k, I_i) - \nu_{i,j}(y_k) < 0\,, \quad i, j = 1, 2 \;\; i \neq j\,. \tag{3}$$

*Sorbonne Université, CNRS, Université de Paris, Laboratoire Jacques-Louis Lions UMR 7598, 75005 Paris, France. (federica.padovano@sorbonne-universite.fr)

†Sorbonne Université, CNRS, Université de Paris, Inria, Laboratoire Jacques-Louis Lions UMR 7598, 75005 Paris, France. (chiara.villa.1@sorbonne-universite.fr)

Under definition (A.18), (3) ensures that F is negative at every y_k $(k = 1, .., K)$ as required by (A.16) and (A.17). In addition, (3) and (A.25) imply

$$\rho_{1k} = \left(\frac{\nu_{2,1}(y_k)}{\nu_{1,2}(y_k) - R_1\big(y_k, I_1\big)} \right) \rho_{2k} = \left(\frac{\nu_{2,1}(y_k) - R_2\big(y_k, I_2\big)}{\nu_{1,2}(y_k)} \right) \rho_{2k} \quad \text{for} \quad k = 1, ..., K\,. \tag{4}$$

For a more precise characterisation of the phenotypic distributions at equilibrium, we must solve (A.20), which is equivalent to simultaneously solving $G = 0$, $\partial_y G = 0$ and $\partial^2_{yy} G \geq 0$. Due to analytical complexity, we here do not solve this explicitly. Instead we investigate the number K of discrete points that we might find solving (A.20), under the specific fitness functions and transition rates, to shed light on the conditions under which we may expect the population to go extinct, present monomorphism or polymorphism at equilibrium.

Let $R_i(y, I_i)$ $(i = 1, 2)$ be given by (7) and $\nu_{i,j}(y)$ $(i, j = 1, 2 \quad i \neq j)$ be given by (9). Note first of all that, under these specific definitions, $G(y, I_1, I_2)$ in (A.19) is a polynomial of order 4 in y. Therefore $\partial^2_{yy} G$ is quadratic in y, suggesting that G can have at most 2 inflection points, determined by solving $\partial^2_{yy} G = 0$ in y. Figure 1 illustrates why in order for the population to be dimorphic we must have 2 inflection points: this will give us a necessary condition for dimorphism and, in the opposite case (*i.e.* if we have one or no inflection points), a sufficient condition for monomorphism – always assuming that the population does not go extinct. Said condition is determined by applying the well-known binomial formula to $\partial^2_{yy} G = 0$ and investigating its discriminant $D(I_1, I_2)$. We here omit simple calculations to derive this and focus on the obtained necessary condition for dimorphism, which is given by

$$D(I_1, I_2) > 0\,. \tag{5}$$

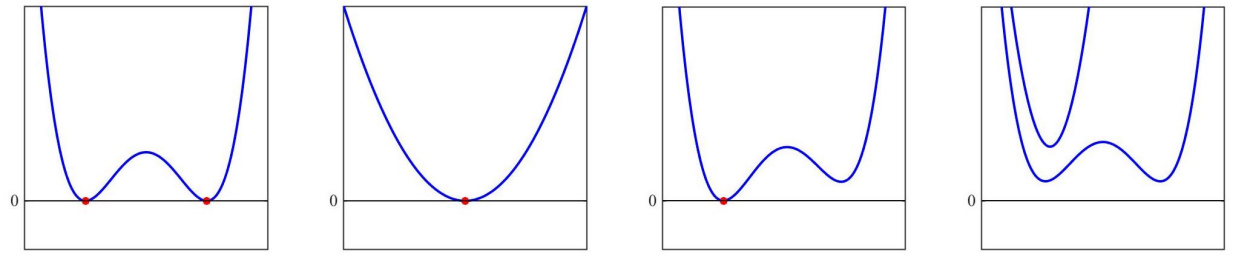

(a) Two points of inflection & dimorphism | **(b) One/No points of inflection & monomorphism** | **(c) Two points of inflection & monomorphism** | **(d) Two/One/No points of inflection & extinction**

Figure 1: **Four different cases for the function G.** Possible plots of $G(y, I_1, I_2)$ as a function of y displaying how G having two inflection points is necessary – cf. (a) and (b) – but not sufficient – *vid* (c) and (d) – for the population to present dimorphism at equilibrium.

Under definitions (7) and (9), condition (5) can be rewritten to give the following condition:

$$(B_1 h_1 - B_2 h_2)^2 + 8 B_1 B V_1 V_2 h_1 h_2 - 2 B_1 B_2 V_1 V_2 (h_1^2 + h_2^2) + 2(1 - V_1 V_2) \left[\frac{a_1 - d_1 I_1}{b_1 + \hat{\nu}_{1,2}} + \frac{a_2 - d_2 I_2}{b_2 + \hat{\nu}_{2,1}} \right] > 0\,,$$

$$\text{with} \qquad B_i := \frac{b_i}{b_i + \hat{\nu}_{i,j}}\,, \qquad V_i := \frac{\hat{\nu}_{i,j}}{b_i + \hat{\nu}_{i,j}} \qquad i, j = 1, 2 \quad i \neq j\,.$$

While this condition is quite complex, we may still consider the limit as $b_1, b_2 \to \infty$, under which we have $B_i \to 1$, $V_i \to 0$ $(i = 1, 2)$ and therefore the condition reduces to $(h_1 - h_2)^2 > 0$, which is satisfied as long as $h_1 \neq h_2$. Therefore under extremely strong selective pressure from the two environments we can – and we might expect to – have dimorphism in both sites, which is in line with the results obtained in the case of constant transition rates. Figure 2 displays the possible model outcomes changing some of the parameters, and obtained simulating a nondimensional version of the model.

2 Supplementary figures

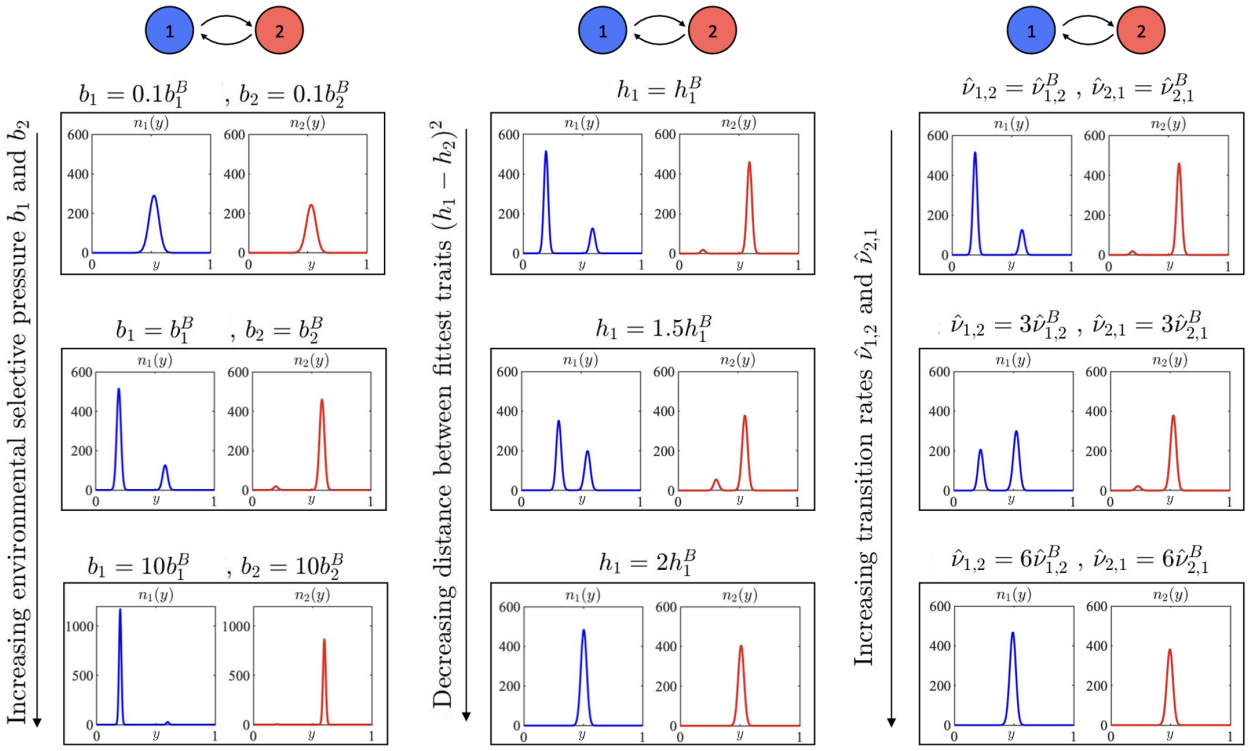

Figure 2: **Outcome dependency on input factors in the secondary seeding scenario.** Illustrative example showing how the selection gradients b_1 and b_2, the fittest trait h_1 and the maximum migration rates $\hat{\nu}_{1,2}$ and $\hat{\nu}_{2,1}$ may affect the equilibrium distributions of the cancer cell populations of each site, in the secondary seeding case. We simulate system (3), under definition (7) for the fitness functions R_i and definition (9) for the migration rates $\nu_{i,j}(y)$, under the initial conditions $n_{0,1}(y) > 0$ and $n_{0,2}(y) = 0$ $\forall y \in [0, 1]$. Each column displays the equilibrium solutions of three simulations obtained by progressively varying the parameters b_1 and b_2 (first column), h_1 (second column) and $\hat{\nu}_{1,2}$ and $\hat{\nu}_{1,,12}$ (third column) form their baseline values $b_2^B = 1$, $b_2^B = 0.6$, $h_1^B = 0.2$, $\hat{\nu}_{1,2}^B = 0.1$ and $\hat{\nu}_{2,1}^B = 0.05$. The remaining parameters are set to $\beta_1 = \beta_2 = 10^{-7}$, $a_1 = 6$, $a_2 = 5$, $b_1 = b_1^B$, $b_2 = b_2^B$, $h_1 = h_1^B$, $h_2 = 0.6$, $d_1 = d_2 = 0.2$, $\hat{\nu}_{1,2} = \hat{\nu}_{1,2}^B$ and $\hat{\nu}_{2,1} = \hat{\nu}_{2,1}^B$.

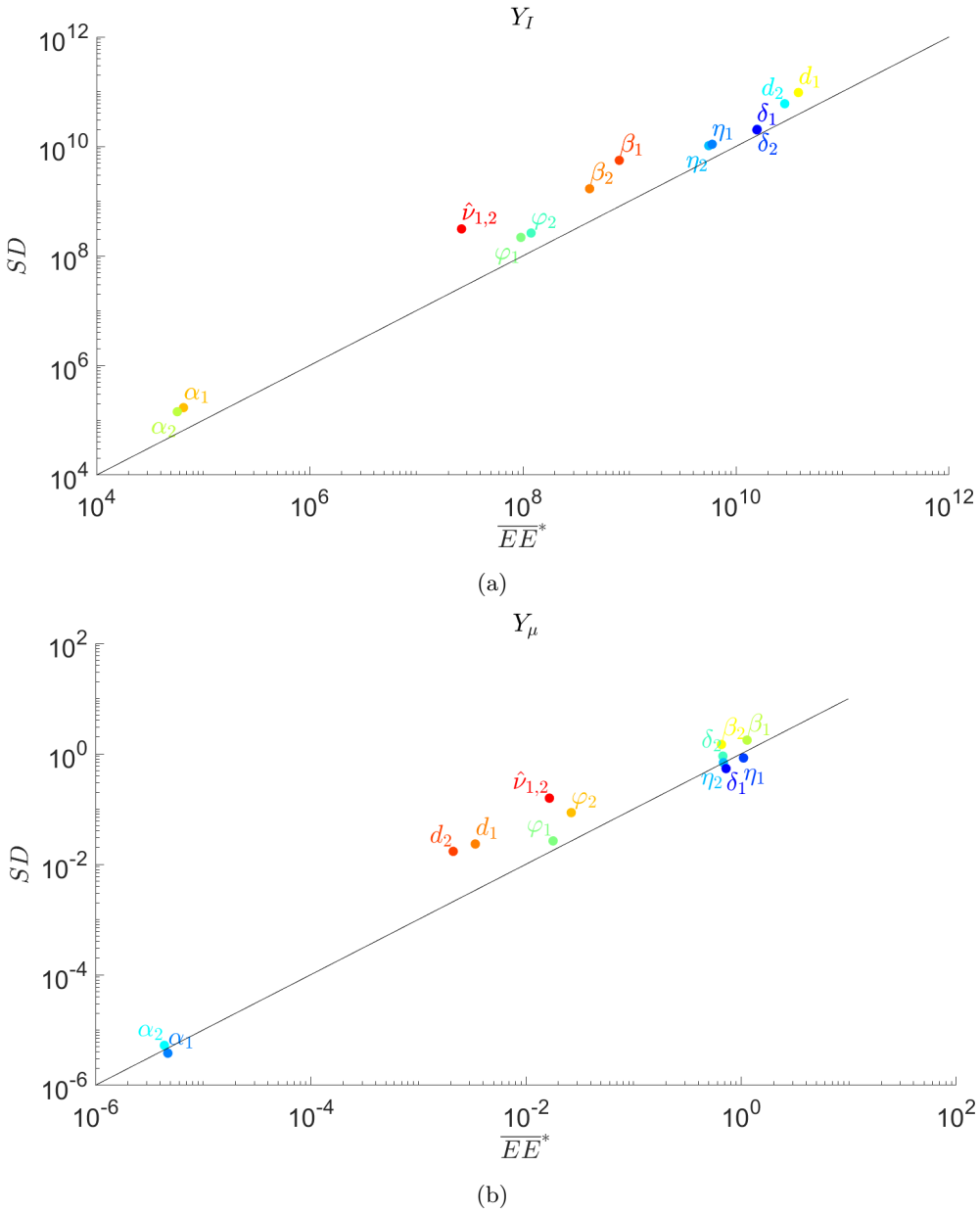

Figure 3: **Results of the Elementary effects method for GSA: EE measures comparison.** Comparison of the EE measures $\overline{EE}_i^*$ (x-axis) and SD_i (y-axis), defined in (37), associated with the model output Y_I (a) and Y_μ (b). The estimates are computed with $r = 500$ evaluations of the elementary effect for each parameter.

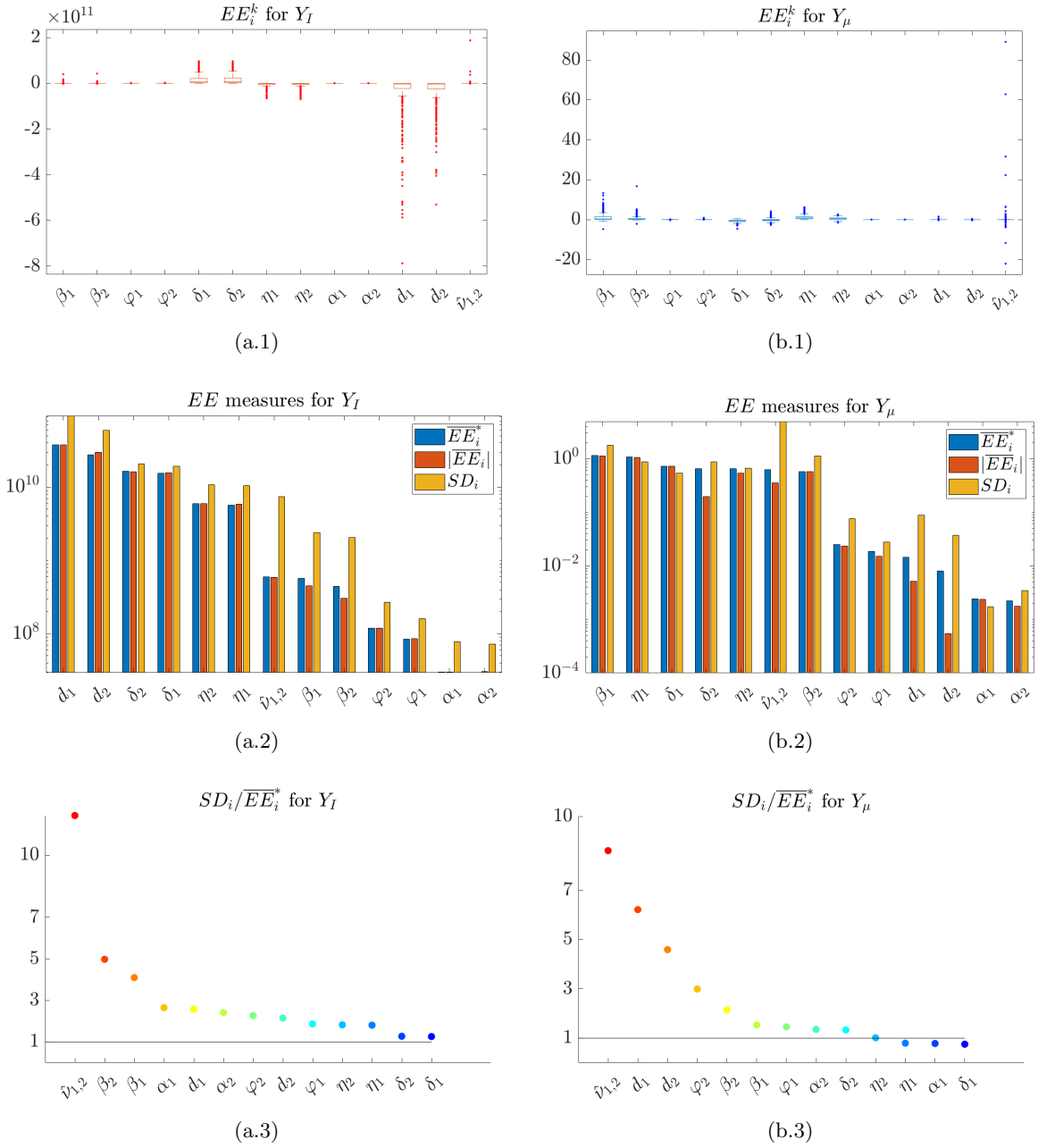

Figure 4: **Results of the Elementary effects method for GSA under a wider range of values for the maximum migration rates.** EE measures associated with the model output Y_I (a.1-3) and Y_μ (b.1-3), *i.e.* the total tumour mass and average mean phenotypic state of the sites. The estimates are computed with $r = 500$ evaluations of the elementary effect for each parameter, and migration rates taking values in the range $\hat{\nu}_{1,2} \in [10^{-13}, 10^{-5}]$ 1/s. The elementary effects EE_i, defined in (36), calculated for each parameter are displayed in plots (a.1) and (b.1). The associated measures $\overline{EE}_i^*$, $|\overline{EE}_i^*|$ and SD_i, defined in (37), are shown in plots (a.2) and (b.2). Plots (a.3) and (b.3) present the ratio between SD and $\overline{EE}_i^*$.

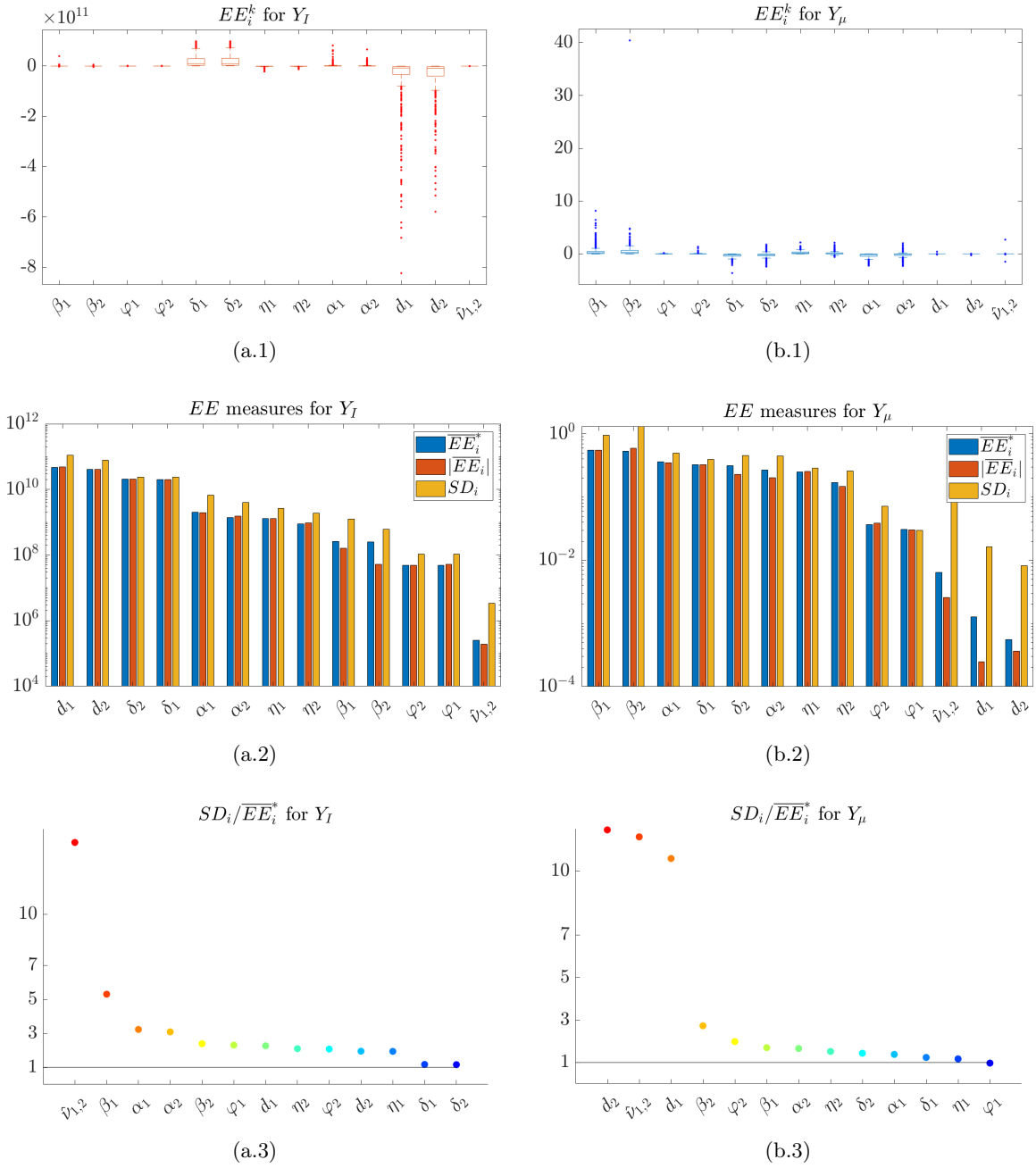

Figure 5: **Results of the Elementary effects method for GSA under a lower drug dose.** EE measures associated with the model output Y_I (a.1-3) and Y_μ (b.1-3), *i.e.* the total tumour mass and average mean phenotypic state of the sites. The estimates are computed with $r = 500$ evaluations of the elementary effect for each parameter, and an intravenously-injected drug dose of $3.75 \cdot 10^{-4}$ $\mu g/s$. The elementary effects EE_i, defined in (36), calculated for each parameter are displayed in plots (a.1) and (b.1). The associated measures $\overline{EE}_i^*$, $|\overline{EE}_i^*|$ and SD_i, defined in (37), are shown in plots (a.1) and (b.2). Plots (a.3) and (b.3) present the ratio between SD and $\overline{EE}_i^*$.

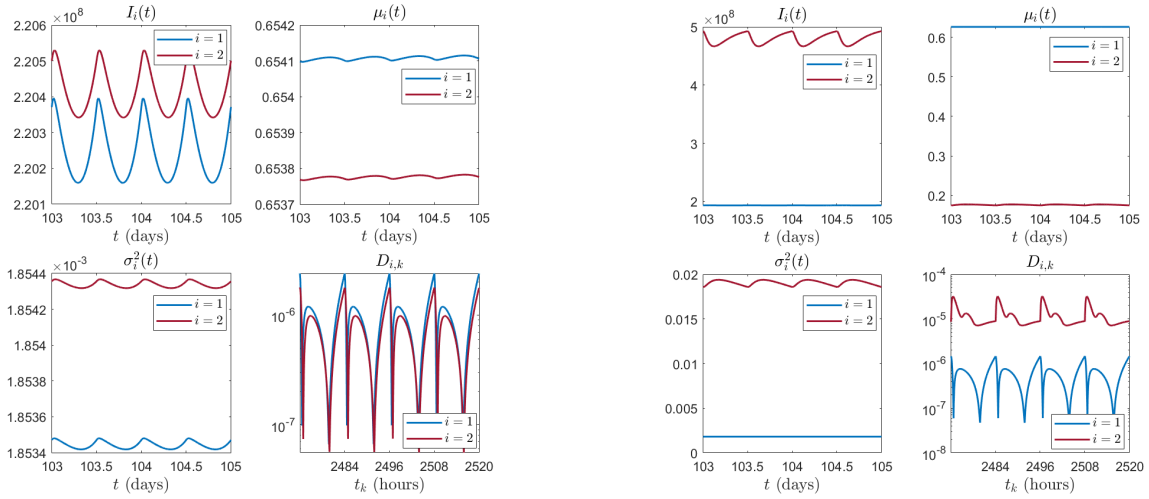

(a) Baseline scenario

(b) Non baseline scenario

Figure 6: **Cancer evolutionary dynamics under baseline and non-baseline scenarios: zoom-in analysis of the last two days of the simulations.** Cancer evolutionary dynamics results of the numerical simulations under the baseline (a) and non-baseline (b) scenarios with the drug schedule of 150 mg orally administered twice a day, and time period $t \in [103, 105]$ days, *i.e.* the last 26301 time steps of the simulation results shown in Figure 7 of the Main Manuscript. For each scenario we plot the population sizes $I_i(t)$ (top left panel), mean phenotypic traits $\mu_i(t)$ (top right panel), the related variances of the phenotypic distributions $\sigma_i^2(t)$ (bottom left panel) and the step differences $D_{i,k}$ (bottom right panel), respectively defined in equations (1), (2) and (35). More details on the simulation set-up and numerical methods can be found in Section 4.1.

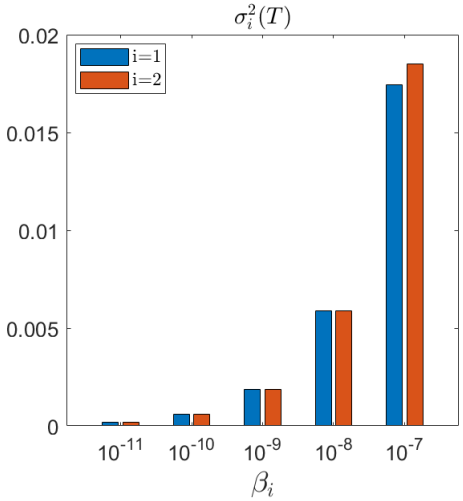

Figure 7: **Variance dependency on β_i.** Treatment outcomes obtained from numerical simulations of the model under the baseline scenario, for an intravenously-injected drug dose of 2.6915 μg/s and a final time of $T = 210$ days. The graph displays the variance σ_i^2, defined in equation (2), of the phenotypic distribution n_i at steady state, varying the epimutation rate β_i. The steady state time is the first time at which $D_{i,k} < tol$, with $D_{i,k}$ defined in (35) and a tolerance of $tol = 10^{-6}$. More details on the simulation set-up and numerical methods can be found in Section 4.1.